

A Modular Deep Learning-based Approach for Diffuse Optical Tomography Reconstruction

Alessandro Benfenati¹, Paola Causin^{2*}, Martina Quinteri²

¹*Department of Environmental Science and Policy, University of
Milano, via Celoria 2, Milano, 20133, Italy.

²Department of Mathematics, University of Milano, via Saldini 50,
Milano, 20133, Italy.

*Corresponding author(s). E-mail(s): paola.causin@unimi.it;
Contributing authors: alessandro.benfenati@unimi.it;
martina.quinteri@studenti.unimi.it;

Abstract

Medical imaging is nowadays a pillar in diagnostics and therapeutic follow-up. Current research tries to integrate established - but ionizing - tomographic techniques with technologies offering reduced radiation exposure. Diffuse Optical Tomography (DOT) uses non-ionizing light in the Near-Infrared (NIR) window to reconstruct optical coefficients in living beings, providing functional indications about the composition of the investigated organ/tissue. Due to predominant light scattering at NIR wavelengths, DOT reconstruction is, however, a severely ill-conditioned inverse problem. Conventional reconstruction approaches show severe weaknesses when dealing also with mildly complex cases and/or are computationally very intensive. In this work we explore deep learning techniques for DOT inversion. Namely, we propose a fully data-driven approach based on a modularity concept: first data and originating signal are separately processed via autoencoders, then the corresponding low-dimensional latent spaces are connected via a bridging network which acts at the same time as a learned regularizer.

Keywords: Diffuse Optical Tomography, Inverse Problems, Deep Learning, Autoencoders, Optical Imaging, Medical Imaging

1 Introduction

Diffuse Optical Tomography (DOT) is an emerging technology which employs light in the NIR spectral window to investigate biological tissues in living beings for diagnostic and monitoring purposes. Its use has been explored in different medical fields, including imaging of brain, thyroid, prostate and breast cancer screening [1–3]. Tomographic reconstruction in DOT aims at recovering the spatial distribution of the tissue optical properties, which can be related to chromophores concentration (mainly water, oxy and deoxy-hemoglobin and, in the case of adipose tissues as breast, lipids) and used to monitor functional changes in blood flow. In DOT technologies, light emitted from external sources at different positions is let to propagate throughout the investigated organ and the emerging photon flux is measured on the tissue boundary [4]. DOT reconstruction is a notoriously severely ill-posed and ill-conditioned inverse problem since at NIR wavelengths the outgoing light consists of a mixture of very few coherent and quasi-coherent photons and a predominant component of incoherent (diffusive) photons which experienced multiple scattering events while crossing the tissue. As such, DOT is intrinsically very sensitive to measurement noise [5].

Model-based image reconstruction approaches have represented in the past the standard strategy to perform DOT reconstruction [1]. They are based on a mathematical model which describes the physics beyond the generation of the measurable quantity on the boundary, and possibly includes also the effect of the acquisition system and the noise affecting the data. Under suitable hypotheses, the reconstruction of the object of interest is achieved by the minimization of a *fit-to-data* functional, which measures the discrepancy between the recorded data and the corresponding quantity computed by the model. The minimization problem is then solved by an optimization algorithm, for example the Gradient Descent or Alternating Direction Method of Multipliers [6].

Due to the ill-conditioned nature of the reconstruction problem, DOT solvers must include a form of regularization, which provides hard or soft prior information on the solution. As for this latter category, the ℓ_2 -norm (Tikhonov/ridge regression) penalization is the benchmark classic regularization approach and has been widely used in DOT literature [7, 8]. The ℓ_1 -norm (lasso) penalization has been also used in this context to improve sharp edges detection, obtained as a by-product of sparsity enhancement [9]. Some of the authors of the present paper proposed in [10, 11] the use of an Elastic-Net regularization term. This approach was investigated both in 2D and 3D domains and provided results superior to the use of pure ℓ_2 or ℓ_1 strategies: the (convex) combination of these norms by the Elastic Net indeed was able to give a satisfactorily stable solution with a preserved sparsity pattern in selected test cases. An alternative approach was proposed in [12], based on Bregman iterations [13]: this iterative technique consists in substituting the regularization function with its Bregman distance from the previous iterate. This procedure, which has been proved to provide a solution to the optimization problem and to possess a remarkable contrast enhancement ability [14, 15], also performs satisfactorily in selected cases in the DOT framework [12]. Other regularization functionals have also been explored in literature, among which we cite here the combined use of a TV method with ℓ_1 -norm in the

TOAST++ software for DOT reconstruction [16]. Nevertheless, despite the amount of the above research work, poor reconstruction results are common outcomes of classical approaches, already in mildly complex situations and/or the reconstruction is too computationally intensive for routinal clinical use. Specifically, a main critical point is the fine tuning of regularization parameters required to obtain a reasonable solution: as a matter of fact, a strong dependence exists on the geometry, mesh-size, optical coefficients distribution and level of noise of each single case, so that a general, effective, strategy is very hard to obtain.

Recently, the outstanding performance on computer vision tasks of deep learning (DL) algorithms based on Neural Networks (NNs), and especially Convolutionary Neural Networks (CNNs), has motivated studies to explore their use also in DOT reconstruction, with the aim to overcome the above discussed shortcomings. The application of DL techniques to DOT is still at its beginnings and very recent: in [17], the so-called SIMBA strategy was proposed: it uses denoising priors, an online extension of classical *Regularization by Denoising* approaches [18–20]; the authors in [21] trained a NN for inverting in an end-to-end fashion the Lippman–Schwinger equation (a model for light propagation in the tissue), by firstly learning the pseudoinverse of the nonlinear mathematical operator, and then applying a downstream network to remove the remaining artifacts. In [22], the authors combined DL with a model-based approach using Gauss–Newton iterations where the update function was learned via a CNN. We refer to the recent work [23] for a review of the other few applications of DL in DOT reconstruction and, more in general, for an overview of the problem, both from the theoretical and computational viewpoints.

In this work, we exploit the nonlinear approximation capabilities of specific deep neural networks, called autoencoders, to perform DOT reconstruction. We propose a modular approach based on the idea of specializing learning tasks for the data and originating signals and putting them together upon a pre-training phase. Namely, first measured data and generating signal are mapped into corresponding feature spaces. Then, these reduced dimensional spaces are connected via a “bridge“ neural operator which connects the latent spaces and at the same time acts as a data-driven regularization operator. This strategy shares conceptual similarities with the learned-SVD approach introduced in [24]. In the present context we provide a thorough analysis of the training strategy which makes this approach modular and efficient. We also draw a parallel with DL-based Reduced Order Modeling techniques for parametrized partial differential equations (see, *e.g.*, [25]), where a latent space of the full order solution is connected with the input parameters and with the neural-network based inversion strategy for electric impedance tomography presented in [26]. In addition, we remark the fact that the idea of learning the regularization via NNs is not new in the general field of inverse problem solution: just to cite a few examples, in [27] a regularization term was learned using only unsupervised data; in [28, 29] a Total Deep Variation functional was learned, while the NETT framework of [30] employs as regularizer the encoder part of an encoder–decoder NN. However, at the best of our knowledge, there are no applications of these concepts in DOT reconstruction.

The paper is organized as follows: in Sect. 2 we introduce the problem and the classical and DL-based approaches. Namely, first we recall the main physical phenomena occurring in light propagation and we introduce the optical coefficients that are the object of DOT reconstruction, then we present mathematical models of light distribution, we define the DOT inverse problem and we present the discrete setting for DOT reconstruction. In Sect. 3 we introduce our DL-based approach, discussing the proposed network architecture, its relations with existing approaches and the training strategy. In Sect. 4 we present extensive numerical experiments and we discuss them; eventually, in Sect. 5 we draw the conclusions of the work.

2 Problem Setting

2.1 Optical properties of biological tissues

The optical properties of biological tissues are the result of their complex internal microstructure, which spans multiple scales and displays a non-homogeneous distribution of the refractive index [31]. In Fig. 1 we schematically depict the main phenomena occurring to a light beam incident on a slice of biological matter, that is, reflection, refraction, absorption and (multi)scattering. Such physical processes can be quantified by a series of parameters, which are presented as coefficients and include the absorption (μ_a) and scattering (μ_s) coefficients and the index of refraction (ν) of the medium.

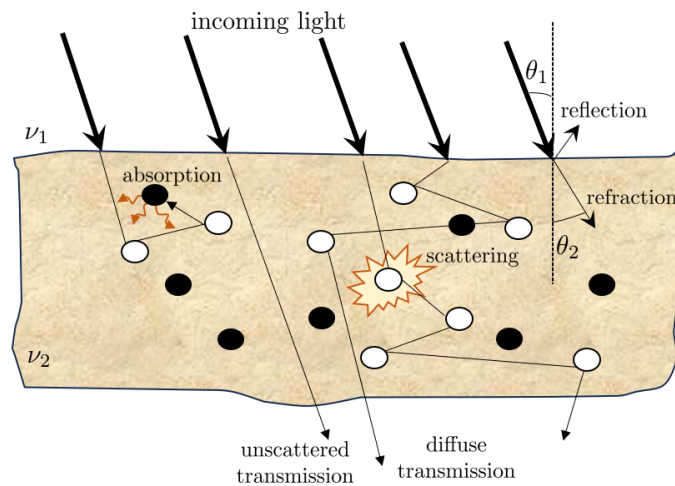


Fig. 1 Biological tissues are complex structures belonging to the class of turbid media with respect to light propagation. An incident light beam may undergo reflection, refraction, absorption and scattering. Of the penetrating photons, only a limited number emerge from the sample via unscattered transmission, the most part of them being instead subjected to multi-scattering events.

Absorption involves the extraction of energy from the photon by chromophores which undergo a transition process (electronic transition or vibrational state transition). Considering a biological medium comprising different chromophores, one can write an equivalent absorption coefficient at wavelength λ , denoted by $\mu_a = \mu_a(\lambda)$, as

$$\mu_a(\lambda) = \sum_i \varepsilon_i(\lambda) C_i, \quad (2.1)$$

where $\varepsilon_i(\lambda)$ and C_i are the absorption extinction coefficient at wavelength λ and concentration of the i -th chromophore, respectively. More specifically, since the main absorbing chromophores in biological tissues are oxy-generated or deoxy-generated haemoglobin, and to a lesser extent water, lipids, melanin, myoglobin, and cytochromes [32], one can rewrite relation (2.1) in the form

$$\mu_a(\lambda) = B (\text{Sat} \cdot \mu_{a,oxy}(\lambda) + (1 - \text{Sat}) \cdot \mu_{a,deoxy}(\lambda)) + W \mu_{a,water}(\lambda) + \sum_{i_{min}} \varepsilon_{i_{min}}(\lambda) C_{i_{min}}, \quad (2.2)$$

where Sat is blood oxygen saturation, B blood volume fraction in the tissue, W water content in the tissue and the sum accounts for other minor absorbers. Diffuse optical imaging typically works in the NIR spectrum since living tissues do not contain strong intrinsic chromophores that absorb radiation in correspondence to that wavelengths and this allows for deeper penetration. In the following, we will assume to collect data on a single NIR frequency and we will write simply μ_a (cm^{-1}), thus omitting the dependence on λ . On the contrary, since we are interested in the spatial distribution of μ_a , we will assume that the distribution of chromophores in the tissue is not homogeneous, so that the absorption coefficient depends on the spatial position \mathbf{r} , *i.e.* $\mu_a = \mu_a(\mathbf{r})$.

Scattering originates from the interaction of photons with structural heterogeneities present inside the biological matter, mainly cellular organelles such as mitochondria, thin fibrillar structures of connective tissues, melanin granules and red blood cells, and from the non-uniform distribution of the refractive index in the medium. The scattering interaction between a photon and a molecule results in the photon moving in a different direction. The NIR window is characterized by the prevalence of elastic scattering, with strong directness upon the collision. Scattering from individual spheres can be calculated from Mie theory [33]; for a medium comprising different types of scatterers one has the equivalent scattering coefficient $\mu_s = \mu_s(\lambda)$ given by

$$\mu_s(\lambda) = \sum_i \rho_i \sigma_i(\lambda), \quad (2.3)$$

where ρ_i is the number density of spheres of the i -th type and $\sigma_i(\lambda)$ the equivalent scattering cross section at wavelength λ . The scattering mean free path $l_s = 1/\mu_s$ represents the average distance a photon travels between consecutive scattering events. The angular distribution of the scattered radiation about the outgoing direction \mathbf{s}' is given by a cone of solid angle $d\mathbf{s}'$ and axis \mathbf{s}' originating at the scatterer at position \mathbf{r} from an incident ray of direction \mathbf{s} (see Fig. 2). Again, in the following we will consider

a fixed λ in the NIR spectrum and we will denote for short the scattering coefficient as μ_s . In the present framework, we assume that μ_s is a known constant throughout the domain.

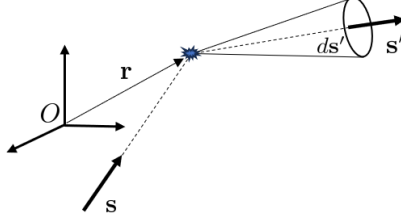


Fig. 2 Scattering in biological tissues causes a ray of light coming from direction \mathbf{s} to be scattered by a particle in position \mathbf{r} in direction \mathbf{s}' around a cone of angle $d\mathbf{s}'$.

Aim of DOT. Imaging by DOT aims at recovering the unknown distribution of optical coefficients in the investigated biological sample illuminated by NIR light sources. Specifically, knowledge of the absorption coefficient field in the tissue can be used to support screening and diagnosis of diseases as cancer or stroke, which are known to alter its physiological distribution due to the accumulation of specific chromophores [34]. Due to relevant technological differences, which directly impact on the reconstruction problem, we specifically focus on DOT based on Steady-State-Domain systems, which are among the most widely used in clinical settings for breast cancer screening, a main field of application of DOT. In this technology, the light is emitted into the tissue at a single frequency (continuous wave modality, CW) and the transmitted luminous signal is measured directly on the tissue boundary or imaged via a CCD camera.

2.2 Mathematical models of light propagation

The mathematical description of the process of light propagation in tissues can be performed via the Maxwell equations or using the theory of radiative transfer (RT) of energy. Models stemming from this latter theory are the most used in optical imaging modalities, since they avoid to deal with the complex statistical nature of the non-homogeneous medium required for the solution of Maxwell equations.

We let $\Omega \subset \mathbb{R}^d$, $d = 2$ or 3 , be a connected open domain representing the tissue to be investigated, and S^{d-1} the unit sphere in \mathbb{R}^d . The main equation of RT reads (at steady-state) [35]

$$(\mathbf{s} \cdot \nabla + (\mu_a(\mathbf{r}) + \mu_s)) I(\mathbf{r}, \mathbf{s}) + \mu_s \int_{S^{d-1}} I(\mathbf{r}, \mathbf{s}') p(\mathbf{s}, \mathbf{s}') d\mathbf{s}' = f(\mathbf{r}), \quad \mathbf{r} \in \Omega, \quad (2.4)$$

where $I = I(\mathbf{r}, \mathbf{s})$ ($\text{W cm}^{-2}\text{sr}^{-1}$) is the radiance at point \mathbf{r} in direction \mathbf{s} , $f(\mathbf{r})$ an internal source term and the scattering phase function $p(\mathbf{s}, \mathbf{s}')$ represents the probability

density function of photon scattering from direction \mathbf{s} to direction \mathbf{s}' . It is common assumption to let the scattering phase function depend only on the angle between the incident and scattered directions, hence to consider it as a function of only the scalar product $(\mathbf{s} \cdot \mathbf{s}')$. In this context, a constant of interest is the cosine-weighted average of the scattering

$$g = \int_{S^{d-1}} p(\mathbf{s}, \mathbf{s}') \mathbf{s} \cdot \mathbf{s}' d\mathbf{s}', \quad g \in [-1, 1]. \quad (2.5)$$

The above quantity is a measure of the forward scattering bias and quantifies how efficiently photons keep propagating in the forward direction despite scatter. When $g = 0$ one has fully isotropic scattering, while when $g \rightarrow 1$ the propagation is strongly forward biased, that is scattering vanishes, and for $g \rightarrow -1$ scattering becomes completely backward directed. For (in vitro) breast tissues at the visible and NIR wavelengths one has typically $0.65 < g < 0.95$ [36].

The RT model (2.4) is an integro-differential equation and its solution is computationally very expensive. A physically reasonable and cost-effective model can be derived by performing an expansion of the RT equation in spherical harmonics (see, e.g., [37] for details and derivation). The following PDE model, known as the diffusion approximation (DA) model, is obtained truncating the expansion at first order:

$$(-\nabla \cdot (D(\mathbf{r})\nabla) + \mu_a(\mathbf{r}))U(\mathbf{r}) = f(\mathbf{r}), \quad \mathbf{r} \in \Omega, \quad (2.6)$$

where the field $U(\mathbf{r}) = \int_{S^{d-1}} I(\mathbf{r}, \mathbf{s}') d\mathbf{s}'$ is the photon fluence due to the light source $f(\mathbf{r})$ and where $D = D(\mathbf{r})$ is the diffusion coefficient given by

$$D(\mathbf{r}) = \frac{1}{3(\mu_a(\mathbf{r}) + (1-g)\mu_s)}, \quad (2.7)$$

with g defined by (2.5). Model (2.6) is equipped with the Robin-type boundary condition

$$U(\mathbf{r}) + \frac{\zeta D(\mathbf{r})}{2c_d} \nabla U(\mathbf{r}) \cdot \mathbf{n} = 0, \quad \mathbf{r} \in \partial\Omega \quad (2.8)$$

where $\zeta = (1 + R)/(1 - R)$, R being a function of the refraction indices ν_1 and ν_2 of the two media concurring at the interface according to the Fresnel law [38], and c_d is a constant depending on the space dimension ($c_d = 1/\pi$ if $d = 2$, $c_d = 1/4$ if $d = 3$).

The Rytov perturbation approach. A common approximation implemented in reconstruction software embedded in CW-DOT instrumentation is the Rytov linearization of the DA model. A complete derivation of this methodology is provided in the general field of line-of-sight wave propagation through random media in Ishimaru [39, Vol. II, Ch. 17] and for the specific DOT application in [40]. In brief, one assumes the linearization $\mu_a(\mathbf{r}) = \mu_{a,0}(\mathbf{r}) + \delta\mu_a(\mathbf{r})$, where $0 < \mu_{a,0} \leq \bar{\mu}_a$ is the background value corresponding to a condition with absence of regions with altered absorption and $\delta\mu_a$ a (small) perturbation term corresponding to a condition with the presence of localized contrast regions with altered - typically increased - absorption coefficient,

the realization of the perturbed status depending on the specific technological setting. An exponential change of variables is also introduced such that

$$U(\mathbf{r}) = U_0(\mathbf{r})e^{\psi_1(\mathbf{r})}, \quad (2.9)$$

where $U_0(\mathbf{r})$ is the light fluence field in background conditions and $\psi_1 = \log(U/U_0)$ is the so-called *logarithmic amplitude fluctuation* of the light due to the presence of contrast regions. Inserting (2.9) into (2.6), performing algebraic manipulations and neglecting higher order terms, yields the following equation for the combined quantity ($U_0\psi_1$)

$$\left[\Delta - \frac{\mu_{a,0}(\mathbf{r})}{D} \right] (U_0\psi_1)(\mathbf{r}) = \frac{\delta\mu_a(\mathbf{r})}{D} U_0(\mathbf{r}), \quad \mathbf{r} \in \Omega. \quad (2.10)$$

Notice that relation (2.10) is obtained under the further assumption of constant diffusion coefficient given by $D = 1/(3\mu_s)$, a simplification which is quite common in the CW-DOT context (see, *e.g.*, [41, 42]).

2.3 DOT inverse problem

We let Q be the function space of optical absorption coefficient given by

$$Q(\mathbf{r}) = \{q(\mathbf{r}) = \mu_a(\mathbf{r}) : 0 < \mu_a(\mathbf{r}) \leq \bar{\mu}_a\}, \quad (2.11)$$

$\bar{\mu}_a$ being a biophysically plausible positive upper bound for the absorption coefficient. Moreover, we let \mathbb{W} represent a (possibly infinite) set of source functions in Ω and W represent the space spanned by the functions in \mathbb{W} . Then, for a particular applied light source $f \in \mathbb{W}$, we denote by $\phi_q = \phi_q(\mathbf{r}; f)$ the state variable belonging to the vector space Φ_q . The field ϕ_q corresponds to the light distribution field in the body due to the light source f , with optical absorption q and is solution of one of the above PDE-type models, of the generic form

$$\begin{aligned} \mathcal{L} \phi_q(\mathbf{r}; f) &= f(\mathbf{r}), \quad \mathbf{r} \in \Omega, \\ \mathcal{B} \phi_q(\mathbf{r}; f) &= 0, \quad \mathbf{r} \in \partial\Omega, \end{aligned} \quad (2.12)$$

where $\mathcal{L} : \Phi_q \times Q \rightarrow W$ is an (integro-) differential operator augmented by a set of boundary conditions represented by the operator \mathcal{B} . Hereafter, we drop the dependence on \mathbf{r} and f to ease the readability. The DOT inverse problem consists in the identification of the set of parameters q , subject to Eq. (2.12), which allow to obtain the best fit with respect to a set of observations of the state variable obtained on (a portion of) the domain boundary. In practice, one disposes of the noisy measurement vector $y_\delta \in Y$, Y being (a possibly infinite) vector space, for some noise level $\delta \geq 0$, obtained via the measurement map $M : \Phi_q \times W \rightarrow Y$ such that

$$y_\delta = M(\phi_q; f) \quad (2.13)$$

represents the measured light field at the observation points. In addition, under suitable assumptions on \mathcal{L} , one can introduce the parameter-to-state map $S : Q \rightarrow \Phi_q$,

i.e. $S(q) = \phi_q$, which is a solution to the boundary value problem (2.12), and define the *forward map* $\mathcal{F} = P \circ S : Q \rightarrow Y$, where P is the observation operator providing the value of the computed solution field at the observations points. Then one aims at computing the best parameter set q^* such that

$$q^* \in \underset{q \in Q}{\operatorname{argmin}} \mathcal{C}(\mathcal{F}(q), y_\delta), \quad (2.14)$$

where $\mathcal{C} : Y \rightarrow [0, +\infty)$ is a cost function. One may take $\mathcal{C}(\mathcal{F}(q), y_\delta) = \|\mathcal{F}(q) - y_\delta\|_{\ell_2}^2$ but also other measures as the Kullback-Leibler divergence are possible choices. Observe that, when Rytov linearization is adopted, upon solving Eq. (2.10), one compares in (2.14) the quantity ψ_1 evaluated at the measurement points with the ratio $\log(y_\delta/y_{0,\delta})$ at the same locations, where light measurements $y_{0,\delta}$ and y_δ correspond to baseline and perturbed conditions, respectively.

As already mentioned, due to predominant scattering phenomena in light transmission, DOT reconstruction (2.14) is a severely ill-posed problem. Mathematically, this means that there is lack of continuous dependence of the solution on the measurements (small errors in the data may lead to large errors in the model parameters). In these circumstances, it becomes essential the adoption of regularization techniques to solve the problem. One possible way is to introduce a regularization term such that the problem becomes: find the optimal parameter set q^* such that

$$q^* \in \underset{q \in Q}{\operatorname{argmin}} [\mathcal{C}(\mathcal{F}(q), y_\delta) + \mathcal{R}(q)], \quad (2.15)$$

where $\mathcal{R} : Q \rightarrow [0, +\infty]$ is a regularization functional which encodes soft or hard prior knowledge about the hidden structures to be investigated, favoring appropriate minimizers or penalizing those with undesired structures [43–45].

2.4 Discrete DOT inverse problem

DOT reconstruction is inherently performed at the discrete level, since in practice one disposes only of a finite set of n_d (possibly noisy) measures of light at the observation points (detectors), obtained when each of the n_s light sources is turned on, for a total of M measures. We denote by $\mathbf{y}_\delta^M \in \mathbb{R}^M$ such set. In addition, also the absorption coefficient is reconstructed in a finite set of locations in the computational domain, typically corresponding to a discretization of the domain into V voxels, with diameter size h . The continuous set of optical coefficients is thus replaced by a finite dimensional set, whose elements $\boldsymbol{\mu}_a^h \in \mathbb{R}^V$ are the approximation of the absorption coefficient value in each voxel.

2.4.1 PDE-based solvers

Classic solvers are based on the solution of the optimization problem (2.14) (or (2.15)). This requires to dispose of: *i*) a computationally efficient method to deal with the PDE system (2.12) which provides the light field for a given set of optical parameters (forward problem); *ii*) an optimization procedure.

As for *i*), the standard approach is to decompose the computational domain into triangular/trapezoidal areas (2D) or into cuboids of suitable shape (3D). Upon introducing a discretization of the domain, one then operates with functions belonging to finite dimensional subspaces parametrized by the mesh diameter h . For example, using a finite elements method, one approximates the solution ϕ_q by a piecewise polynomial function $\phi_{q,h} \in \Phi_h$ given by

$$\phi_{q,h} = \sum_{j=1}^{N_h} \phi_j \xi_j(\mathbf{r}), \quad (2.16)$$

where Φ_h is a finite dimensional subspace (typically chosen such that $\Phi_{q,h} \subset \Phi_q$) spanned by the basis functions $\{\xi_j\}_{j=1,\dots,N_h}$ and where the nodal values ϕ_j are to be determined. Piecewise polynomial approximation to the optical absorption coefficient, $\boldsymbol{\mu}_a^h$, is constructed in the same way. Applying a Galerkin approach transforms the continuous problem into the N_h -dimensional discrete problem of finding the nodal field values at all nodes, given the set of nodal parameters.

As for *ii*), supposing that the forward map \mathcal{F} is Fréchet differentiable, a Taylor expansion around a reference point q_0 reads

$$\mathcal{F}(q) \approx \mathcal{F}(q_0) + \mathcal{F}'(q_0)\delta q, \quad \delta q = q - q_0 \quad (2.17)$$

where \mathcal{F}' is the first order Fréchet derivative of the forward operator with respect to q . Inserting (2.17) into (2.14) and truncating to the first order yields, upon discretization of the fields and using directly the increment $\delta\boldsymbol{\mu}_a^h$

$$(\delta\boldsymbol{\mu}_a^h)^* \in \underset{\delta\boldsymbol{\mu}_a^h}{\operatorname{argmin}}[\mathcal{C}(\mathbf{J}\delta\boldsymbol{\mu}_a^h, \mathbf{y}_\delta^M) + \mathcal{R}(\delta\boldsymbol{\mu}_a^h)], \quad (2.18)$$

where \mathbf{J} of size $M \times V$ denotes in the discrete setting the first order Fréchet derivative (Jacobian matrix) and where $\delta\boldsymbol{\mu}_a^h$ is the voxel-based increment for the unknown optical field. The optimization problem (2.18) can be solved by one of the many available algorithms (see [23] for a review).

3 Learning DOT reconstruction via Neural Networks

We discuss in this section our original contribution. We aim to find an approximate solution to DOT reconstruction leveraging the approximation capabilities of nonlinear neural networks. Namely, we introduce neural networks which produce mappings of the type

$$\mathcal{N} : \mathbb{R}^M \rightarrow \mathbb{R}^V \quad (3.1)$$

and perform data-driven reconstruction of the optical coefficient from observations. The architecture we propose is characterized by the two autoencoder networks

$$\begin{aligned} \text{data-AE} : \Psi_y : \mathbb{R}^M &\rightarrow \mathbb{R}^M, \\ \text{signal-AE} : \Psi_\mu : \mathbb{R}^V &\rightarrow \mathbb{R}^V. \end{aligned} \quad (3.2)$$

The data-AE acts on observations \mathbf{y}_δ^M and is defined by $\Psi_y = \mathcal{D}_y \circ \mathcal{E}_y$, with

$$\begin{aligned} \mathbf{z}_y &= \mathcal{E}_y(\mathbf{y}_\delta^M) \quad \mathcal{E}_y : \mathbb{R}^M \rightarrow \mathbb{R}^{n_y} && \text{(encoder)} \\ \tilde{\mathbf{y}}_\delta^M &= \mathcal{D}_y(\mathbf{z}_y), \quad \mathcal{D}_y : \mathbb{R}^{n_y} \rightarrow \mathbb{R}^M && \text{(decoder)}, \end{aligned} \quad (3.3)$$

where \mathbf{z}_y is the encoded feature (latent or compressed representation) of the data and $\tilde{\mathbf{y}}^M$ its decoded version. The signal-AE acts on the generating signal \mathbf{y}_δ^M and is defined by $\Psi_\mu = \mathcal{D}_\mu \circ \mathcal{E}_\mu$, with

$$\begin{aligned} \mathbf{z}_\mu &= \mathcal{E}_\mu(\boldsymbol{\mu}_a^h) \quad \mathcal{E}_\mu : \mathbb{R}^{N_h} \rightarrow \mathbb{R}^{n_\mu} && \text{(encoder)} \\ \tilde{\boldsymbol{\mu}}_a^h &= \mathcal{D}_\mu(\mathbf{z}_\mu), \quad \mathcal{D}_\mu : \mathbb{R}^{n_\mu} \rightarrow \mathbb{R}^{N_h} && \text{(decoder)}, \end{aligned} \quad (3.4)$$

where \mathbf{z}_μ is the encoded generating signal and $\tilde{\boldsymbol{\mu}}_a^h$ its decoded version. In addition, we introduce a third network, called bridge-NN, which has the role to connect (as a bridge) the two previous latent spaces

$$\Sigma : \mathbb{R}^{n_y} \rightarrow \mathbb{R}^{n_\mu}. \quad (3.5)$$

The proposed DL-based DOT reconstruction is thus defined by the following structure (called Mod-DOT):

$$\mathcal{N} := \mathcal{D}_\mu \circ \Sigma \circ \mathcal{E}_y : \mathbb{R}^M \rightarrow \mathbb{R}^V. \quad (3.6)$$

Remark 1. *The proposed architecture is articulated into three modules which serve to different purposes: the two AEs are deputed to learn the intrinsic characteristics of the data and signal manifolds, respectively. Their specificity is tailored to handle the different richness of the respective inputs. The bridge needs instead to learn the effect-to-cause relation between observation and generating signal in the reduced spaces. A schematic representation of the proposed architecture is given in Fig. 3.*

The Mod-DOT neural architecture. We detail here the AE and bridge architectures used for compressing the data and originating signal manifolds and to approximate the inversion operator.

- *data-AE:* predominant scatter in the tissue severely hinders the collection of data that show neat differences even for well distinct internal distributions of the absorption coefficient. This results into very similar data patterns generated by different samples. For this reason, this autoencoder is deliberately chosen to be very simple. In this architecture, the smoothing effect typical of autoencoders provides an initial denoising of the measures. Both encoder and decoder part are chosen to be made of fully connected layers coupled with `tanh` and sigmoid activation functions, respectively;
- *signal-AE:* generating signal samples are provided under the form of images which encode the absorption coefficient field. In the images, contrast areas of altered (increased) absorption are embedded into a background value. The richness of this input is definitely higher than the observations. The resulting architectures are schematized in Fig. 4, where the inputs and outputs are also represented. For the

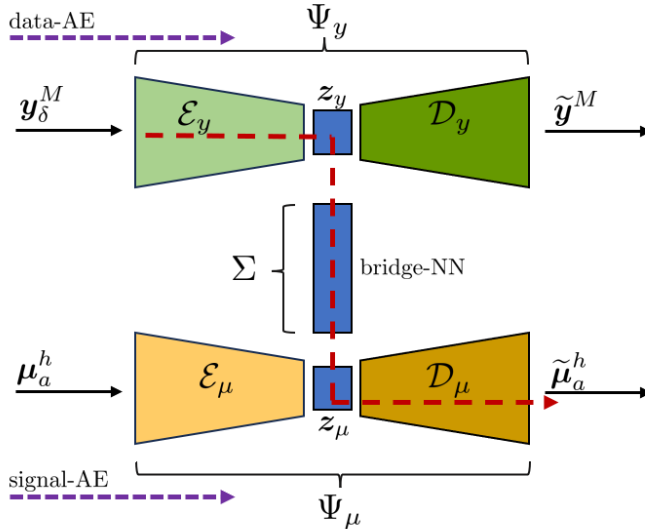


Fig. 3 Workflow in the Mod-DOT approach. Observed data and originating signal are encoded individually in the corresponding latent spaces via the data-AE and the signal-AE, respectively (violet arrow paths). Latent spaces are then connected via the bridge-NN. At test time, the reconstruction process consists in the cascade application of the three networks (red arrow path) $\mathcal{N} := \mathcal{D}_\mu \circ \Sigma \circ \mathcal{E}_y$.

data-AE, the input is represented by the DOT “sinogram”, where observations collected at the detectors locations for each light source are represented as a vector. For the signal-AE, the input is represented by the absorption coefficient field in the form of an image or a vector. In the figure, we represent the case where the net is presented with a one-channel image in which the dark blue region represents the background value, while the two circular regions are contrast areas with increased absorption coefficient (see also Sect. 4.1 for more detailed description).

- *bridge-NN*: the bridge networks connects the data and signal latent spaces, performing the core of the inversion. Fully connected dense layers are adopted in order to effectively perform this operation.

Related data-driven approaches. The full bridged structure finds a remarkable interpretation as a learned SVD strategy (see [24] for its original introduction). To understand this concept, it is useful to draw a parallel with the physical models introduced in Sect. 2.2: one may decompose the linearized discrete parameter-to-state operator as $\mathbf{J} = \mathbf{U}\mathbf{S}\mathbf{V}^\top$, where \mathbf{S} is the diagonal matrix containing the singular values and \mathbf{U} and \mathbf{V} are the left and right singular vectors, respectively, and express the solution via the inversion formula $\mathbf{J}^{-1} = \mathbf{V}\mathbf{S}^{-1}\mathbf{U}^\top$. This fundamental idea of linear algebra is extended via neural networks to more general nonlinear parameter-to-state operators, which are not formally derived from a model but directly learnt from data. Namely, one learns a generalized SVD decomposition via the AE architectures. In this framework, the encoder \mathcal{E}_y can be seen as the corresponding of \mathbf{U}^\top and the decoder \mathcal{D}_μ

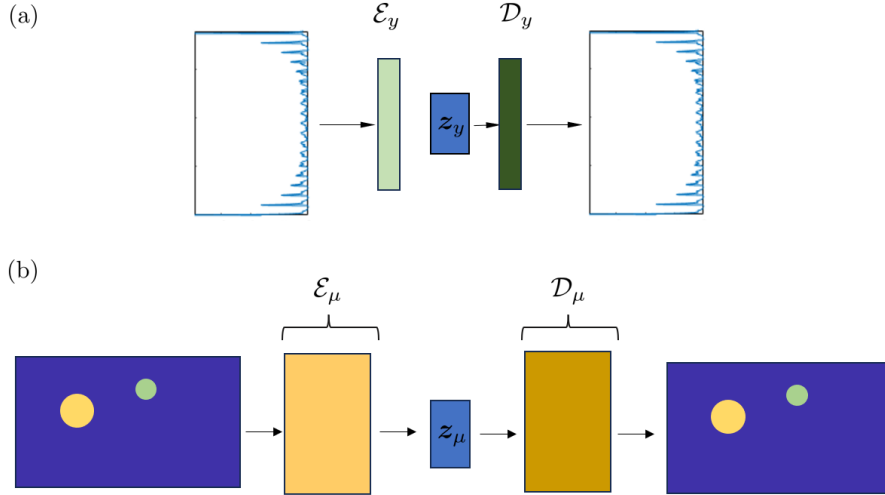


Fig. 4 Architecture of the AEs: (a) the data-AE receives in input the DOT “sinogram“ composed by the collection of all the light observations at the detectors locations for each source and it is trained to reproduce the identity operator on it; (b) the signal-AE receives in input the absorption coefficient field, presented here as a one-channel image where the circular areas represent contrast regions with increased coefficient. It is trained to reproduce the identity operator on the image.

can be considered as the counterpart of \mathbf{V} . The bridging operator Σ , which relates the latent spaces in the data and signal domains, plays the mapping and scaling role of the singular values in \mathbf{S} in the linear algebraic SVD approach. This parallelism is visually represented by the following scheme:

$$\begin{array}{ccccc}
 \mathbf{y}_\delta^M & \xrightarrow{\mathcal{E}_y} & \mathbf{z}_y & \xrightarrow{\mathcal{D}_y} & \tilde{\mathbf{y}}^M \\
 & & \downarrow \Sigma & & \\
 \boldsymbol{\mu}_a^h & \xrightarrow{\mathcal{E}_\mu} & \mathbf{z}_\mu & \xrightarrow{\mathcal{D}_\mu} & \tilde{\boldsymbol{\mu}}_a^h
 \end{array} \quad (3.7)$$

Noticeably, the bridging operator also acts as a regularizer of the inversion. To understand this point, it is useful to recall the classic inversion by Tikhonov regularization, which is obtained from (2.15) when \mathcal{C} is the least square functional and \mathcal{R} is the ℓ_2 norm of its argument (bound on the variance of the solution). Upon linearization and discretization, one obtains a problem of the type

$$(\delta \mathbf{q}^h)^* \in \underset{\delta \mathbf{q}^h \in Q^h}{\operatorname{argmin}} \|\mathbf{b} - \mathbf{J} \delta \mathbf{q}^h\|_{\ell_2}^2 + \alpha \|\delta \mathbf{q}^h\|_{\ell_2}^2 = \mathbf{V} \underbrace{(\mathbf{S}^2 + \alpha \operatorname{Id})^{-1} \mathbf{S} \mathbf{U}^T \mathbf{b}}_{\mathbf{S}_\alpha^{-1}}, \quad (3.8)$$

where \mathbf{b} stands for the right hand side and α is a regularization parameter. The diagonal elements of \mathbf{S}_α^{-1} , defined as $\frac{\sigma}{\sigma^2 + \alpha}$, filter out the smallest singular values,

according to the threshold α . This can be interpreted as a smoothed Truncated SVD, where the singular values go towards zero in a smooth fashion, which mitigates noise in the data, enhanced by the smallest singular values at the denominator. Truncated SVD, instead, puts to zero the singular values after k terms. Drawing the parallel, the nonlinear SVD obtained by the neural network learns from the data the operator Σ and automatically doses the amount of required regularization. In doing so, it learns at the same time the regularization functional \mathcal{R} and the parameter α , which are both encompassed in Σ .

A second remarkable tie of the present architecture can be found with Reduced Order Modeling (ROM) techniques applied to the solution of parametric partial differential equations of type (2.12). Conventional ROM techniques rely on the assumption that the reduced order approximation can be expressed by a linear combination of basis functions, built from a set of full order solutions. Namely, first one computes for different values of the parameters the so-called Full Order Method (FOM) snapshots. Then, for example considering the Principal Orthogonal Decomposition (POD) approach, one writes the FOM snapshots as columns of a matrix $\mathbf{A} := [\phi_{q_1}^h, \phi_{q_2}^h, \dots, \phi_{q_N}^h]$ and computes its SVD decomposition $\mathbf{A} = \mathbf{U}\mathbf{S}\mathbf{V}^\top$. The low-dimensional representation of the solution is taken as the projection $\phi_q^{LR} := \mathbf{V}^\top \phi_q^h$ and then one needs an algorithm that approximates the correspondence $\mathbf{q}^h \rightarrow \phi_q^{LR}$, usually via a reduced map θ such that $\phi_q^{LR} \approx \theta(\mathbf{q}^h)$. This map has been chosen in literature in different ways, including Gaussian process regression and polynomial chaos expansion (see [25] and references therein). Eventually, one reconstructs $\phi_q^h \approx V\theta(\mathbf{q}^h)$. The resulting ROM manifold is thus linear and its dimension can become extremely high and/or produce inaccurate results for problems involving nonlinearities. Recently, approaches have emerged where the solution map is approximated by a deep neural network, yielding the so-called DL-ROM methods [25]. Adapting the notation of this latter paper to the one used in the present work for ease of readability, a typical DL-ROM is inspired by the steps of the classical ROM and it encompasses the three networks $\mathcal{E}_\phi, \mathcal{D}_\phi$ and Σ_ϕ such that

$$\mathcal{E}_\phi(\phi_q^h) = \mathbf{z}_\phi, \quad \mathcal{D}_\phi(\mathbf{z}_\phi) = \tilde{\phi}_q^h \approx \phi_q^h, \quad \Sigma_\phi(\mathbf{q}^h) \approx \mathbf{z}_\phi, \quad (3.9)$$

where \mathcal{E}_ϕ is an encoder which produces the latent space \mathbf{z}_ϕ - conceptually corresponding to the low resolution representation ϕ_q^{LR} -, \mathcal{D}_ϕ decodes back the latent space into the solution manifold and Σ_ϕ is a dense network which produces the parameter-to-solution operator. Eventually, one has $\mathcal{N}_\phi := \mathcal{D}_\phi \circ \Sigma_\phi : Q_h \rightarrow \Phi_h$ such that $\tilde{\phi}_q^h = \mathcal{D}_\phi(\Sigma_\phi(\mathbf{q}^h)) \approx \phi_q^h$. We schematically depict in Fig. 5 the corresponding architecture. It is thus apparent that both the Mod-DOT and DL-ROM share similarities in the use of specialized modules connecting low dimensional spaces. Observe, however, that the DL-ROM aims to solve - in the form presented in [25] - the *forward* problem for values of the parameters in correspondence of which a FOM solution is not available due to the high computational cost needed to explore a wide range of parameters. As such, the direction of the workflow of the DL-ROM at test time is the

opposite with respect to the one for the inverse problem we consider in our application (compare for reference the red arrows in Fig. 3 and Fig. 5). We are not aware of the use of DL-ROM techniques in our context.

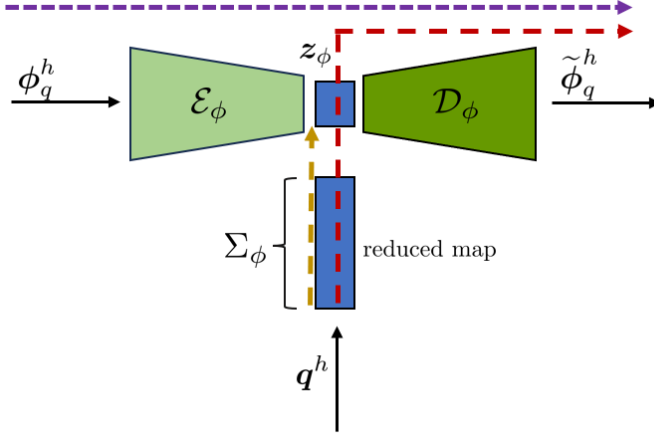


Fig. 5 Workflow in the DL-ROM approach (here shown for comparison with the present approach). First, the AE $\mathcal{D}_\phi \circ \mathcal{E}_\phi$ is trained to learn an approximation of the identity operator over the solution manifold (violet arrow) using FOM snapshots obtained by a computationally intensive computation. This AE provides the latent low-dimensional representation z_ϕ of the solution manifold. Then, the network Σ_ϕ is trained to learn the map $q^h \rightarrow z_\phi$ (dark yellow arrow). Finally, the composition $\mathcal{D}_\phi \circ \Sigma_\phi$ defines the DL-ROM approximation of the parameter-to-state map at test time (red arrow).

A further connection of the present architecture can be found with the strategy proposed in [26] for the reconstruction of the conductivity field from voltage measurements in electric impedance tomography (EIT), another notoriously ill-posed inverse problem. As in our approach, instead of using a net which directly reconstructs in an end-to-end fashion the conductivity field from the voltages, first a AE is trained to learn the identity operator on the originating signal (conductivity presented as images) and then a nonlinear regression map is learned to connect the measured obtained from the AE. This latter net is expected to deal with a significantly better conditioned problem. Adapting also in this case the notation of [26] to the present one, we have

$$\mathcal{E}_q(q^h) = z_q, \quad \mathcal{D}_q(z_q) = \tilde{q}^h \approx q^h, \quad \Sigma_q(\phi_q^h) \approx z_q, \quad (3.10)$$

where \mathcal{E}_q is an encoder which produces the latent space z_q from the signal manifold, \mathcal{D}_q decodes back z_q into the signal manifold and Σ_q is a regression map which approximates the measure-to-parameter operator. In this case, one has $\mathcal{N}_q := \mathcal{D}_q \circ \Sigma_q$. Theoretical support of the usefulness to work with low-dimensional non-linear manifolds for the signal images is provided in [26] based on the result that the inverse problem in EIT with sufficiently many measures is uniquely solvable and Lipschitz

stable on finite dimensional linear subsets of piecewise-analytic functions. This motivates the idea that realistic originating signal fields lie on a non-linear manifold that is lower dimensional than the space of all possible images.

4 Numerical experiments

In the following we assess the performance of the proposed Mod-DOT approach. For comparison, we also consider classic variational approaches and an End-to-End NN, called E2E-DOT, which consists in the simple juxtaposition of the data encoder and the signal decoder, without bridge, that is $\mathcal{N}_{E2E} = \mathcal{D}_\mu \circ \mathcal{E}_y$, and mimics end-to-end approaches already present in literature to address DOT reconstruction.

4.1 Generation of synthetic data

We consider synthetic data on 2D domains (a semi-disk or a rectangle) in which circular contrast regions of random size, absorption intensity and position are embedded (see Fig. 6). Light sources are positioned at constant intervals on the bottom side, 1 mm inside the domain, so to that they are considered as volume sources. This is clearly an approximation, but it is sufficiently accurate for the present scopes. On this same part of the domain, null boundary conditions are enforced for the light field to represent the physical plate in which lights are embedded. The detectors are positioned on the left, top and right parts of the domain for the rectangular shape and on the curved portion of the domain for the semi-disk. To train the network, we generated a set of 1500 samples, each including one or two circular contrast regions with random radius and position inside the domain. The contrast regions were chosen to have absorption coefficient equal to 3, 4 or 5-fold the background coefficient. When there were two contrast regions, each region was allowed to have different absorption coefficient. The test dataset used to evaluate the performance of the proposed architecture and to compare it with other approaches contained 150 samples built according to the same rules as above. Observations are, where specified, polluted with Gaussian noise (1% to 5% with respect to the local value). Measures of light fluence at the detectors locations are generated by solving the DA model (2.6) via a quadratic Finite Element code implemented via an in-house software in MATLAB using a small discretization parameter for high resolution. We consider 9000 train samples. The parameters used in the numerical tests are listed in Tab. 1. Fig. 7 shows some examples of the absorption coefficient fields along with the corresponding DOT sinograms computed by the FEM code for the rectangular domain. Notice again how the light fluence measures obtained for different absorption fields are very similar: they have indeed a maximal point-to-point difference of 10^{-4} , which makes the reconstruction problem very hard.

We consider 150 test samples for evaluation. To assess the performance of the algorithms by first labeling in the reconstructed signal image the voxels belonging to the contrast region. To do this, the image is binarized and the connected components are labeled out. Then, we evaluate the following indices:

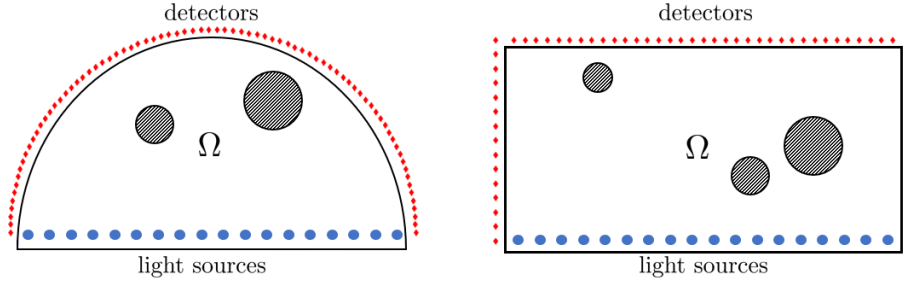


Fig. 6 Geometry of the semi-disk and rectangular domains considered in the numerical experiments. The detectors are uniformly disposed along the curved boundary for the semi-disk and top/left/right boundary for the rectangle domain; the sources are aligned along the bottom boundary and positioned 1mm inside the domain. The absorption coefficient is $\mu_{a,0}$ except for the contrast regions (circular areas) which have increased absorption coefficient.

Table 1 Parameter values used in the generation of the synthetic data

Name	Symbol	Value	Units
domain size (rectangle)		10×5	cm
domain size (semi-disk)		radius 5	cm
max radius of contrast region		1.0	cm
min radius of contrast region		0.5	cm
background absorption coeff	$\mu_{a,0}$	0.01	cm^{-1}
contrast region absorption coeff		$(3 \text{ to } 5) \times \mu_{a,0}$	
scattering coeff	μ_s	0.1 to 1	cm^{-1}
no. of sources	n_s	19	
no. of detectors	n_d	200	

I_1 : True Positive Ratio (*TPR*). For each test sample, it is given by

$$TPR = \frac{\text{True Positives}}{\text{True Positives} + \text{False Negatives}},$$

where True Positives are the number of voxels in which the algorithm correctly recognized the contrast region, while False Negatives are the number of voxels in which the algorithm did not recognize the presence of a contrast region existing in the ground truth

I_2 : Absolute Bias Error (*ABE*). For each test sample, it is given by

$$ABE = \frac{1}{V} \sum_{i=1}^V |\mu_{a,GT}^{h,i} - \mu_a^{h,i}|$$

where $\mu_{a,GT}^{h,i}$ is the ground truth coefficient evaluated at the voxel

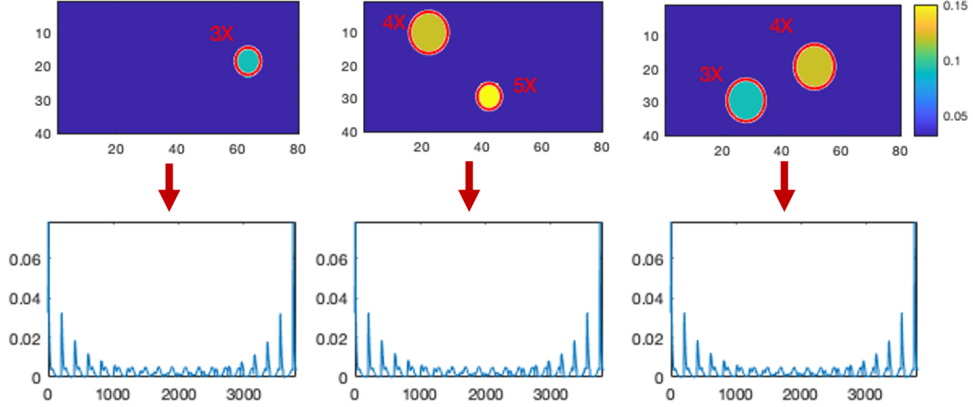


Fig. 7 Examples of synthetic fields of absorption coefficient (top row) along with the corresponding computed DOT sinogram (bottom row) in the rectangular domain. Contrast regions display an increased absorption coefficient, indicated by the red label, with respect to the background value. The values are presented as μ_a/D , the red circles denote the ground truth contrast regions.

I_3 : Structural Similarity Index (*SSIM*). This is a perceptual metric that is usually adopted in video industry to quantify image quality degradation caused by processing such as data compression or by losses in data transmission. Luminance, contrast and structure are the three parameters that are included in its definition (see [46] for its definition and computation in the radiology field).

4.2 Implementation of the neural networks

In this section we outline the structure of the networks implemented for the Mod-DOT and E2D-DOT structures.

- *data-AE*: it is a compact architecture which receives in input the sinogram y_δ^M of dimension 3800(= 200×19). Its encoder part \mathcal{E}_y consists of a single fully connected (FC) layer with a hyperbolic tangent activation function. The generated latent space has size 800. The decoder part \mathcal{D}_y also features a single fully connected (FC) layer with a Sigmoid activation function. It takes an 800-dimensional input vector and generates a 3800-dimensional output vector. In total, the data-AE encompasses 6,084,600 trainable parameters.
- *signal-AE*: it is a richer architecture which takes in input images of dimension 40×80 (or equivalently vectors of size 3200) describing the absorption coefficient field. For its construction, we conducted numerous experiments with different architectures and dimensions. Eventually, we considered two versions, one with fully connected layers and one with convolutional layers. which are described in detail in Tab.2. This encoder generates a bottleneck with dimension 800 ($4 \times 10 \times 20$), equal to the dimension of the latent space of the data-AE. Again, this latter choice is the result of various experiments.

Name	Layer type	Output shape	kernel size	stride	padding	dilation
\mathcal{E}_μ^1	Conv2d	[-1, 16, 40, 80]	(3, 3)	(1, 1)	(1, 1)	-
\mathcal{E}_μ^2	ReLU	[-1, 16, 40, 80]	-	-	-	-
\mathcal{E}_μ^3	MaxPool2d	[-1, 16, 20, 40]	2	2	-	1
\mathcal{E}_μ^4	Conv2d	[-1, 8, 20, 40]	(3, 3)	(1, 1)	(1, 1)	-
\mathcal{E}_μ^5	ReLU	[-1, 8, 20, 40]	-	-	-	-
\mathcal{E}_μ^6	MaxPool2d	[-1, 8, 20, 40]	2	2	-	1
\mathcal{E}_μ^7	Conv2d	[-1, 4, 10, 20]	(3, 3)	(1, 1)	(1, 1)	-
\mathcal{E}_μ^8	ReLU	[-1, 4, 10, 20]	-	-	-	-
\mathcal{D}_μ^1	ConvTranspose2d	[-1, 8, 20, 40]	(2, 2)	(2, 2)	-	-
\mathcal{D}_μ^2	ReLU	[-1, 8, 20, 40]	-	-	-	-
\mathcal{D}_μ^3	ConvTranspose2d	[-1, 16, 40, 80]	(2, 2)	(2, 2)	-	-
\mathcal{D}_μ^4	ReLU	[-1, 16, 40, 80]	-	-	-	-
\mathcal{D}_μ^5	ConvTranspose2d	[-1, 1, 40, 80]	(3, 3)	(1, 1)	(1, 1)	-
\mathcal{D}_μ^6	Sigmoid	[-1, 1, 40, 80]	-	-	-	-

Table 2 Structure of the signal-AE with convolutional layers. In total, there are 2421 trainable parameters. The first 8 layers compose the encoder, the remaining the decoder.

- *bridge-NN*: it is a network composed of seven fully connected layers with hyperbolic tangent activation functions. Each layer has the same input and output dimensions of 800. This network has 4,485,600 trainable parameters
- *denoiser NN*: both the Mod-DOT and E2D-DOT nets were complemented with a downstream network based on convolutional layers which helps in removing the remaining artifacts upon inversion. The network architecture, called DEN, is described in Tab. 3. In total, it comprises 185,217 trainable parameters.

4.2.1 Training strategy

According to the modular philosophy adopted for the Mod-DOT architecture, a decoupled or partially decoupled training strategy is suggested. This approach allows to take advantage of intrinsic regularities in the data and signal manifolds, as discussed above. First, the two AEs are trained separately, in a sort of pre-train phase, then the trained weights of the encoder \mathcal{E}_y and of the decoder \mathcal{D}_μ are used as initial guess to train the complete bridged network $\mathcal{N} = \mathcal{D}_\mu \circ \Sigma \circ \mathcal{E}_y$. The utility of the pre-train phase has been assessed via an extensive experimentation, and it is especially evident for the signal-AE component. On the contrary, the bridge is trained in a coupled fashion with the pre-trained portions of the two AEs. Observe that an analogous decoupled strategy is used also in the DL-ROM approach for the AE part. On the contrary with respect to our approach, in the DL-ROM method also the reduced map is trained separately.

Name	Layer type	Output shape	kernel size	stride	padding
DEN_1	Conv2d	$[-1, 32, 40, 80]$	$(3, 3)$	$(1, 1)$	<i>same</i>
DEN_2	LeakyReLU	$[-1, 32, 40, 80]$	-	-	-
DEN_3	Conv2d	$[-1, 64, 40, 80]$	$(3, 3)$	$(1, 1)$	<i>same</i>
DEN_4	LeakyReLU	$[-1, 64, 40, 80]$	-	-	-
DEN_5	Conv2d	$[-1, 128, 40, 80]$	$(3, 3)$	$(1, 1)$	<i>same</i>
DEN_6	LeakyReLU	$[-1, 128, 40, 80]$	-	-	-
DEN_7	ConvTranspose2d	$[-1, 64, 40, 80]$	$(3, 3)$	$(1, 1)$	$(1, 1)$
DEN_8	LeakyReLU	$[-1, 64, 40, 80]$	-	-	-
DEN_9	ConvTranspose2d	$[-1, 32, 40, 80]$	$(3, 3)$	$(1, 1)$	$(1, 1)$
DEN_{10}	LeakyReLU	$[-1, 32, 40, 80]$	-	-	-
DEN_{11}	ConvTranspose2d	$[-1, 1, 40, 80]$	$(3, 3)$	$(1, 1)$	$(1, 1)$
DEN_{12}	LeakyReLU	$[-1, 1, 40, 80]$	-	-	-

Table 3 Structure of the denoising network based on convolutional layers.

We have however observed that in the case of the solution of the inverse problem, a fully decoupled approach like this latter does not yield satisfactory results, since the bridge-NN (which conceptually corresponds to the reduced map) has to approximate a very complex map to bridge the latent spaces. For pre-training, we used the Adam optimizer, batch size 64, and learning rate 5×10^{-5} . The number of epochs was set to 500 for the data-AE and 10000 for the signal-AE. For both the AEs, we used the Means Square Error cost function.

In the training phase of both the Mod-DOT and E2D-DOT networks, 10000 epochs were used to allow for prolonged learning periods, considering the complexity of the target to achieve. A batch size of 64 was utilized for each iteration, and the dataset was shuffled at the start of every epoch. The Adam optimization algorithm was employed with learning rate 5×10^{-5} .

Unlike the pretraining networks, various choices for the loss function were investigated, and, namely, we considered the following options ($\#N$ is the number of samples):

- (a) mean square error: $loss_{MSE} = \frac{1}{\#N} \sum_{i=1}^{\#N} [\mathcal{N}(\mathbf{y}_{\delta,i}^M) - \boldsymbol{\mu}_{a,i}^h]^2$
- (b) mean square error + ℓ_1 norm for feature selection (with α regularization parameter):
- $$loss_{MSE+\ell_1} = \frac{1}{\#N} \sum_{i=1}^{\#N} [\mathcal{N}(\mathbf{y}_{\delta,i}^M) - \boldsymbol{\mu}_{a,i}^h]^2 + \alpha \sum_{i=1}^{\#N} [\mathcal{N}(\mathbf{y}_{\delta,i}^M) - \boldsymbol{\mu}_{a,i}^h]$$

(c) mean square error + control on AE error:

$$loss_{MSE+AE} = \frac{1}{\#N} \sum_{i=1}^{\#N} [\mathcal{N}(\mathbf{y}_{\delta,i}^M) - \boldsymbol{\mu}_{a,i}^h]^2 + [\Psi_y(\mathbf{y}_{\delta,i}^M) - \mathbf{y}_{\delta,i}^M]^2 + [\Psi_\mu(\boldsymbol{\mu}_{a,i}^h) - \boldsymbol{\mu}_{a,i}^h]^2$$

All the considered neural networks have been implemented in the `pytorch` framework. Computations have been run on the HPC cluster INDACO owned by University of Milano, equipped with Nvidia A100 GPUs (2.3GHz, 32 cores, 1TB RAM).

4.3 Implementation of the classic variational approaches

In order to compare the performance of the proposed NN approach with classic methods, we consider two strategies based on the Rytov linearization using different regularization procedures:

- Elastic Net regularization [10]: we solve the problem

$$(\boldsymbol{\delta}\boldsymbol{\mu}_a^h)^* \in \operatorname{argmin}_{\boldsymbol{\delta}\boldsymbol{\mu}_a^h} \frac{1}{2} \|\mathbf{J}\boldsymbol{\delta}\boldsymbol{\mu}_a - \mathbf{b}\| + \alpha \left(\vartheta \|\boldsymbol{\delta}\boldsymbol{\mu}_a^h\|_1 + (1 - \vartheta) \|\boldsymbol{\delta}\boldsymbol{\mu}_a^h\|_2^2 \right), \quad (4.1)$$

where the regularizer is a convex combination of the ℓ_2 and ℓ_1 norms, with $\vartheta \in [0, 1]$. This approach aims at combining the sparse-promoting and peak-enhancing property of the ℓ_1 norm and the robustness of the Tikhonov regularization. The solution is computed using the MATLAB implementation of `glmnet` [47], a highly efficient package that fits generalized linear and similar models via penalized maximum likelihood. Cross validation is used to obtain the optimal regularization parameter

- Bregman iterations [12, 15]: this is a strategy where at each step where the regularization operator is substituted by its the Bregman Divergence computed at the previous iterate. If \mathcal{R} satisfies suitable hypotheses (namely, being a convex, proper, lower semicontinuous function) and denoting by $\partial\mathcal{R}(\boldsymbol{\xi})$ the subdifferential of \mathcal{R} computed at $\boldsymbol{\xi}$ (see [48] for technical details), then the Bregman divergence of \mathcal{R} is given by

$$D_{\mathcal{R}}^{\mathbf{p}}(\boldsymbol{\xi}, \boldsymbol{\eta}) = \mathcal{R}(\boldsymbol{\xi}) - \mathcal{R}(\boldsymbol{\eta}) - \langle \mathbf{p}, \boldsymbol{\xi} - \boldsymbol{\eta} \rangle, \quad \mathbf{p} \in \partial\mathcal{R}(\boldsymbol{\xi}),$$

where $\mathbf{p}^k \in \partial\mathcal{R}(\boldsymbol{\delta}\boldsymbol{\mu}_a^k)$. An iterative procedure is used, such that the functional to be minimized at the $(k+1)$ -th step is given by

$$\begin{cases} \boldsymbol{\delta}\boldsymbol{\mu}_a^{k+1} \in \operatorname{argmin}_{\boldsymbol{\delta}\boldsymbol{\mu}_a^h} \frac{1}{2} \|\mathbf{J}\boldsymbol{\delta}\boldsymbol{\mu}_a^h - \mathbf{b}\|_2^2 + \alpha D_{\mathcal{R}}^{\mathbf{p}^k}(\boldsymbol{\delta}\boldsymbol{\mu}_a^h, \boldsymbol{\delta}\boldsymbol{\mu}_a^k) - \alpha \langle \mathbf{p}^k, \boldsymbol{\delta}\boldsymbol{\mu}_a^h \rangle \\ \mathbf{p}^{k+1} = \mathbf{p}^k - \frac{1}{\alpha} \mathbf{J}^\top (\mathbf{J}\boldsymbol{\delta}\boldsymbol{\mu}_a^h - \mathbf{b}). \end{cases} \quad (4.2)$$

The above Bregman procedure is coupled with the choice of ℓ_1 regularization.

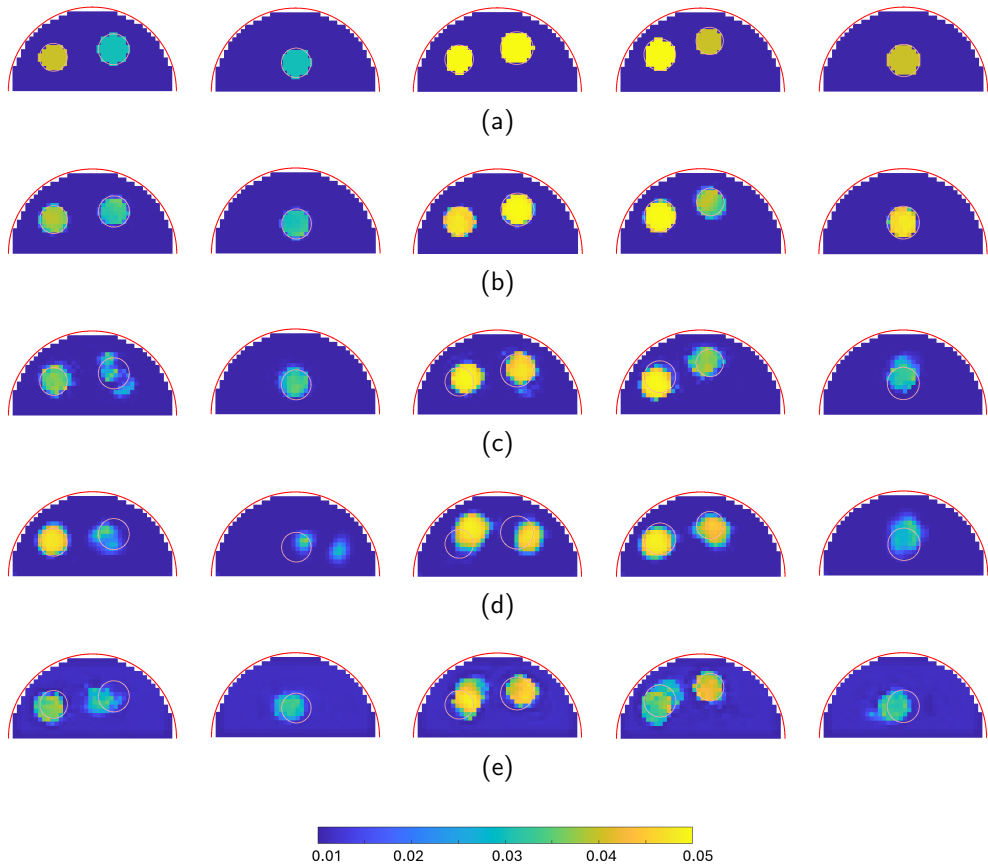


Fig. 8 Reconstruction of the absorption coefficient distribution obtained with the Mod-DOT approach. (8a) Ground truth. The red circles denote the true contrast regions along with the corresponding absorption coefficient, expressed as a multiplier of the background value. (a): noiseless data; (b): 1% noise; (c): 3% noise; (d): 5% noise. The red circles denote the ground truth contrast regions.

4.4 Numerical results: qualitative and quantitative evaluation

4.4.1 Comparison of Mod-DOT vs classic approaches

We consider for this study the semi-disk geometry and we compare the performance of the Mod-DOT approach with fully connected layers in the signal-AE vs the reconstruction obtained by the Elastic Net and Bregman iterations approaches. Fig. 8 presents the absorption coefficient reconstructed by the Mod-DOT for five different test (unseen) samples in the test set with varying levels of noise. In each figure, the red circles depict the ground truth contrast regions. With noiseless data (second row of Fig. 8), the contrast region is almost perfectly recovered, both in location, shape and intensity. The successive rows refer to the reconstruction obtained when Gaussian noise pollutes the data. As it is to be expected, increasing noise levels worsen the overall quality of the reconstruction, even if the gross location and shape of the perturbed region are still correctly captured. Fig. 9 (Elastic-Net) and Fig. 10 (Bregman) show

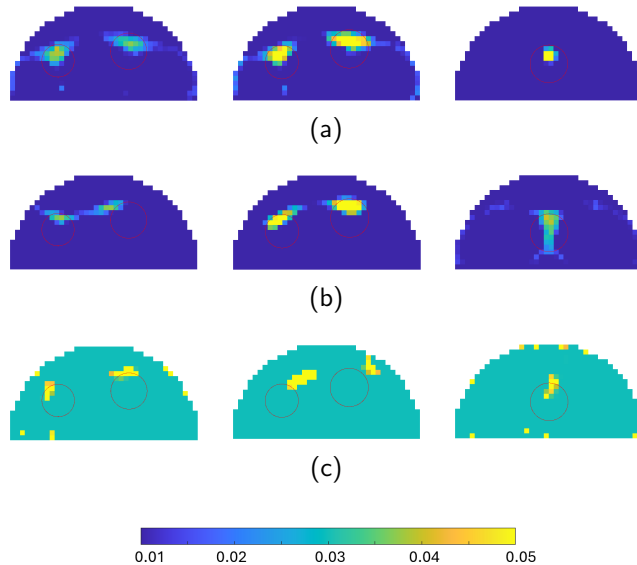


Fig. 9 Reconstruction via the Elastic Net approach of the test samples of columns 1, 3 and 5 in Fig. 8a. (a): noiseless data; (b): 1% noise; (c): 3% noise. The red circles denote the ground truth contrast regions.

the results corresponding to the test samples of columns 1, 3 and 5 in Fig. 8a. Observe as already in the noiseless case (first row) both these classic methods do not achieve a good reconstruction. As the noise level increases the reconstruction quality further deteriorates, so that noise level 5% is not reported here for the classic methods due to complete lack of significance. Simulations performed reducing the voxel size, from the original 0.25 cm, in the reconstruction show partially improved, although this does not solve the difficulty in handling noisy data.

We summarize in Tab. 4 the ACR and TPR metrics for this test case. The table presents the averages on the 150 samples of the test set for the Mod-DOT approach and, for comparison, for the two considered classic approaches. Notice that the ACR results have been binned according to the intensity of the contrast region. For all the approaches, increasing levels of noise significantly worsen the TPR, as well as the ACR. However, the Mod-DOT reconstruction is significantly less affected by quality loss. The contrast regions reconstructed with this approach still show a notable contrast with respect to the background value, and 46% of the extension of the perturbed regions is correctly recovered on average even for the highest noise level (vs 5% and 3% for the variational approaches, respectively). One should notice that in the Elastic Net approach the reconstructed intensities constantly approximate the nominal one by defect for low noise level: this is not fully surprising, since regularization comes at the cost of a certain degree of smearing/blurring of the solution. The approach based on Bregman iterations increase the contrast, as already observed in previous works, although it struggles with noisy data.

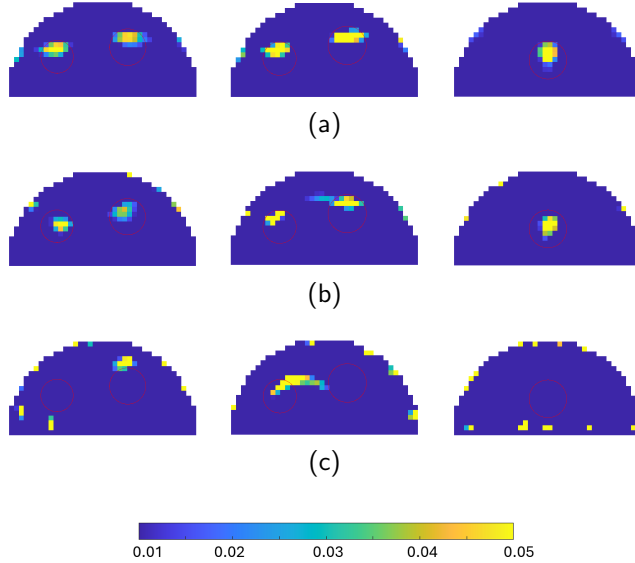


Fig. 10 Reconstruction via the Bregman approach. (a): noiseless data; (b): 1% noise; (c): 3% noise. The red circles denote the ground truth contrast regions.

4.4.2 Comparison of networks with fully connected vs convolutional layers

In this study we show that convolutive layers perform better than fully connected layers in the signal-AE, especially when using noisy data for DOT reconstruction. With this aim, we consider the rectangular geometry with circular contrast regions of different size, location and intensity. In this case the absorption coefficient samples are presented to the nets as 80×40 images. Training is carried out as specified above. We study the performance metrics both for the E2E and Mod-DOT approaches. In each case, we apply denoising and we consider the loss function which gives best results. Tab. 5 refers to the noiseless case, while Tab. 6 refers to the noisy data. It is apparent that in the noiseless case there is no evident advantage to use convolutive layers in terms of the metrics. The number of parameters is, however, always in favour of the convolutive filters. For example, the Mod-DOT-FC architecture has 10,274,817 parameters while the Mod-DOT-CONV architecture has 7,712,426 parameters. The difference is more relevant when we consider noisy data. As a matter of fact, not only the version of the net with convolutive filters has less parameters, but also the metrics show a better quality of the reconstruction. Based on these findings, in the following studies we always adopt a signal-AE based on convolutive layers.

4.4.3 Comparison of Mod-DOT vs E2E architectures

We compare in this study the Mod-DOT and the corresponding E2E architecture. Notice that the E2E architecture represents a typical end-to-end neural network-based workflow for problem inversion. In the context of DOT reconstruction, it is comparable to the architectures used in the recent literature works [49–51]. We consider the same

noise	$3\mu_{a,0}$ (GT: 3e-2)	$4\mu_{a,0}$ (GT: 4e-2)	$5\mu_{a,0}$ (GT: 5e-2)	TPR
Mod-DOT				
0%	$3.05e-02 \pm 2.00e-03$	$4.08e-02 \pm 3.72e-03$	$4.74e-02 \pm 2.19e-03$	0.94
1%	$3.07e-02 \pm 2.77e-03$	$3.76e-02 \pm 5.54e-03$	$4.38e-02 \pm 4.01e-03$	0.76
3%	$3.06e-02 \pm 5.56e-03$	$3.61e-02 \pm 6.10e-03$	$4.11e-02 \pm 4.65e-03$	0.52
5%	$3.00e-02 \pm 3.82e-03$	$3.15e-02 \pm 4.44e-03$	$3.39e-02 \pm 6.04e-03$	0.46
Elastic Net				
0%	$2.73e-02 \pm 4.74e-03$	$3.45e-02 \pm 4.96e-03$	$3.90e-02 \pm 8.69e-03$	0.45
1%	$2.91e-02 \pm 9.36e-03$	$4.30e-02 \pm 8.70e-03$	$5.01e-02 \pm 9.80e-03$	0.17
3%	$9.55e-02 \pm 1.92e-02$	$1.25e-01 \pm 2.83e-02$	$1.23e-01 \pm 3.36e-02$	0.05
Bregman				
0%	$4.02e-02 \pm 8.95e-03$	$5.93e-02 \pm 1.61e-02$	$8.54e-02 \pm 2.98e-02$	0.26
1%	$4.77e-02 \pm 1.81e-02$	$5.85e-02 \pm 1.84e-02$	$8.34e-02 \pm 2.85e-02$	0.17
3%	$1.28e-01 \pm 5.50e-02$	$1.45e-01 \pm 9.06e-02$	$1.36e-01 \pm 6.80e-02$	0.03

Table 4 ACR (binned according to the intensity of the contrast region) and TPR metrics for different noise levels. Values are averaged over 150 test samples.

structure	ABE	MSE	TPR	SSIM
E2E - FC (MSE+L1)	$1.08974 \cdot 10^{-3}$	$3.87490 \cdot 10^{-5}$	0.93115	0.98792
Mod-DOT - FC (MSE+L1)	$1.55653 \cdot 10^{-3}$	$8.72685 \cdot 10^{-5}$	0.88245	0.97509
E2E - CONV (MSE)	$1.11889 \cdot 10^{-3}$	$3.60208 \cdot 10^{-5}$	0.92200	0.98850
Mod-DOT - CONV (MSE+L1)	$1.60053 \cdot 10^{-3}$	$9.59041 \cdot 10^{-5}$	0.86057	0.97317

Table 5 Performance metrics for the different architectures we consider. For each method it is specified the loss function which performs better. FC=fully connected, CONV=convolutional layers.

structure	noise	ABE	MSE	TPR	SSIM
E2E - FC (MSE+L1)	1%	$9.0472 \cdot 10^{-3}$	$5.8909 \cdot 10^{-4}$	0.7939	0.8275
	3%	$1.3144 \cdot 10^{-2}$	$9.3043 \cdot 10^{-4}$	0.7627	0.7586
	5%	$1.3882 \cdot 10^{-2}$	$9.4602 \cdot 10^{-4}$	0.6722	0.7497
Mod-DOT - FC (MSE+L1)	1%	$2.3437 \cdot 10^{-3}$	$1.4226 \cdot 10^{-4}$	0.7925	0.9592
	3%	$3.2026 \cdot 10^{-3}$	$2.2142 \cdot 10^{-4}$	0.7152	0.9424
	5%	$4.2008 \cdot 10^{-3}$	$2.8598 \cdot 10^{-4}$	0.6988	0.9217
E2E - CONV (TOT)	1%	$4.55500 \cdot 10^{-3}$	$2.82388 \cdot 10^{-4}$	0.7054	0.9287
	3%	$1.55794 \cdot 10^{-2}$	$1.08184 \cdot 10^{-3}$	0.5339	0.7707
	5%	$1.41335 \cdot 10^{-2}$	$1.08453 \cdot 10^{-3}$	0.6160	0.7624
Mod-DOT - CONV (MSE)	1%	$2.17595 \cdot 10^{-3}$	$1.42636 \cdot 10^{-4}$	0.81388	0.96252
	3%	$2.83007 \cdot 10^{-3}$	$1.99531 \cdot 10^{-4}$	0.73764	0.94974
	5%	$3.25266 \cdot 10^{-3}$	$2.41429 \cdot 10^{-4}$	0.71242	0.94322

Table 6 Performance metrics for the different architectures we consider. For each method it is specified the loss function which performs better. FC=fully connected, CONV=convolutional layers.

domain as in the previous section and we assess the performance of the two architectures based on 150 test (unseen) samples. We first consider noiseless data, then we consider noisy data as in the previous study. Noticeably, the E2E architecture outperforms the Mod-DOT when we use noiseless data (see Fig. 11), while the Mod-DOT architecture is superior when considering noisy, more realistic, data (see Fig. 12).

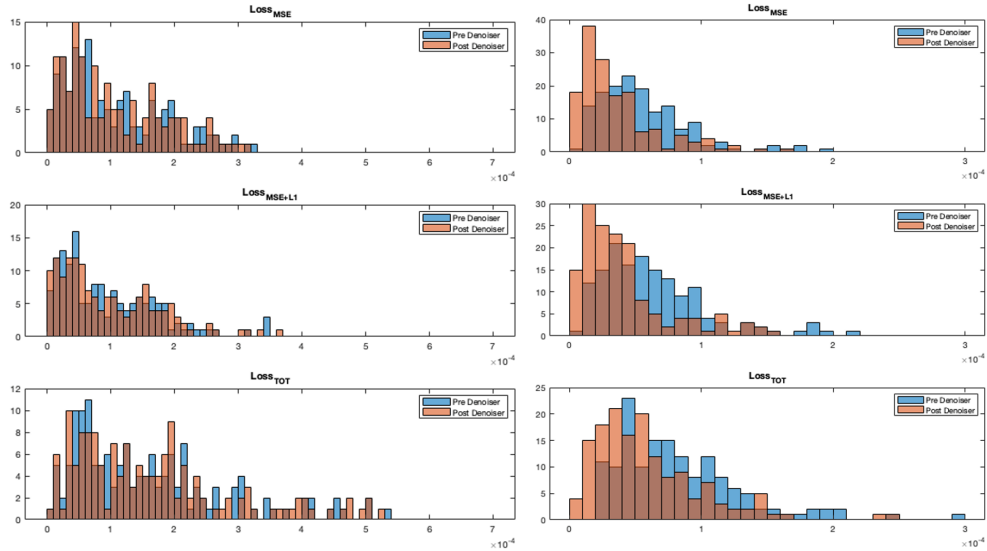


Fig. 11 Histogram of the MSE obtained from 150 test samples. The reconstruction is obtained via the E2E (left column) vs Mod-DOT architecture (right column) with noiseless data and after passage through the denoising network. The superposed histograms in each figure represent the MSE before (light blue bars) and after (orange bars) passing through the denoising network. The rows correspond to the different choices of the loss function as discussed in Sect. 4.2.1. Note that the ranges of the graphs in each column are different for better readability.

4.4.4 Study of training strategies

We investigate the effect of the training strategy on the accuracy of the results. Namely, we compare the reconstructed images by the E2E (Fig. 13) and Mod-DOT architectures (Fig. 14) when training is performed monolithically on the net or the two AEs are first pre-trained and then the net is trained in a coupled fashion. It is apparent that for increasing noise, pretraining the AEs, and especially the signal-AE, yields superior results for both architectures.

4.4.5 Study of out-of-distribution test samples

We conclude our analysis by considering again the rectangular geometry and we try to reconstruct with the Mod-DOT net absorption images with elliptical contrast regions. The net has been trained only on samples with circular contrast regions and we present

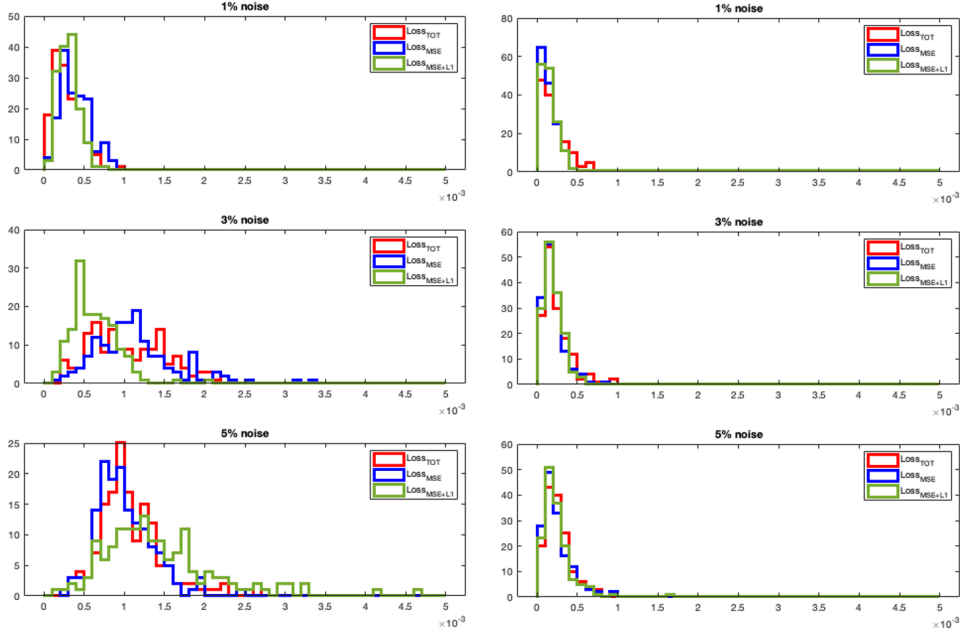


Fig. 12 Histogram of the MSE obtained from 150 test samples. The reconstruction is obtained via the E2E (left column) vs Mod-DOT architecture (right column) with noisy data and after passage through the denoising network. The rows correspond to the different noise levels, while colors in each graph correspond to different choices of the loss function. Note that the ranges of the graphs are different for better readability.

it with test samples having contrast regions made of ellipses with different location, size and orientation of the axes. We show in Fig. 15 the reconstructed images of the absorption coefficient for 3 different test samples. In general, the net is able to qualitatively reconstruct the correct location and intensity of the contrast regions. The shape of the region is not always correctly reconstructed. Observe, however, that training only on circular regions imposes a strong bias on the shape. In addition, the sinograms obtained with the elliptical contrast regions are minimally different from those obtained from circular contrast regions (first two columns in Fig. 15). There are samples where the reconstruction has a lower quality (third column in Fig. 15). This may depend on the sinogram generated by a certain distribution of the coefficient, even it is not easy to establish a general criterion.

5 Conclusion

DOT reconstruction is a severely ill-conditioned problem which demands a careful treatment. Commonly used strategies are based on physics-driven models accompanied by priors which enforce constraints on the variance of the solution or in its sparsity. These strategies often fail or are computationally very intensive. In this work, we have investigated a data-driven approach based on a modular use of neural networks

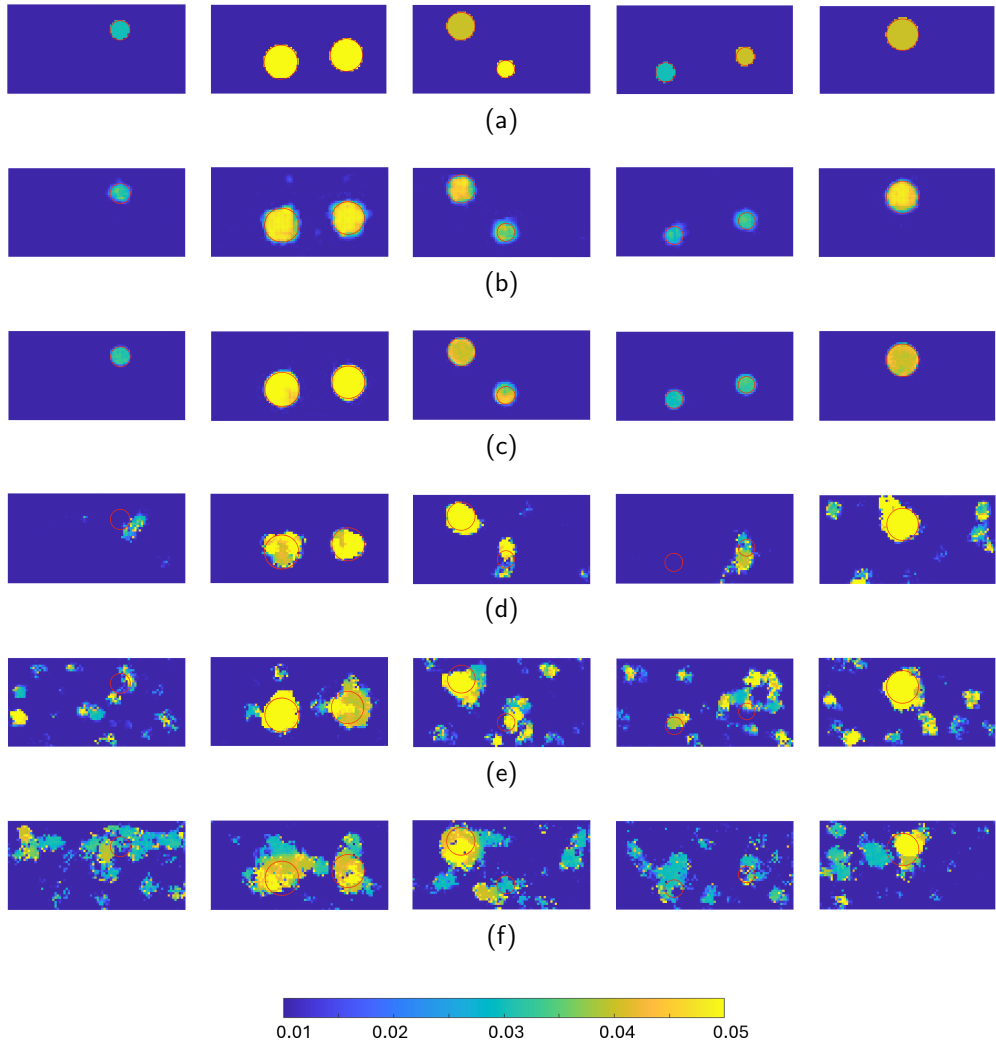


Fig. 13 Reconstruction of the absorption coefficient distribution obtained with the E2E approach. (a): ground truth; (b): reconstruction without pretraining the AEs, before the application of the denoiser; (c): reconstruction with pretraining of the AEs before denoising; (d): reconstruction with pretraining of the AEs after denoising. (e): 1% noise; (f): 3% noise; (g): 5% noise. Rows (e) to (g) use pretrain and denoising. Values are presented as μ_a/D , the red circles denote the true contrast regions.

which exploits the use of autoencoders. This architecture, called Mod-DOT, shares common elements with the Learned-SVD method originally proposed in [24] for general inverse problems, with the DL-ROM methods for parametrized partial differential equations and with the inversion strategy for EIT proposed in [26]. Specifically, our approach shares the idea to exploit the reduced dimension latent spaces obtained via an autoencoder to improve the quality of the reconstruction. At the same time, the

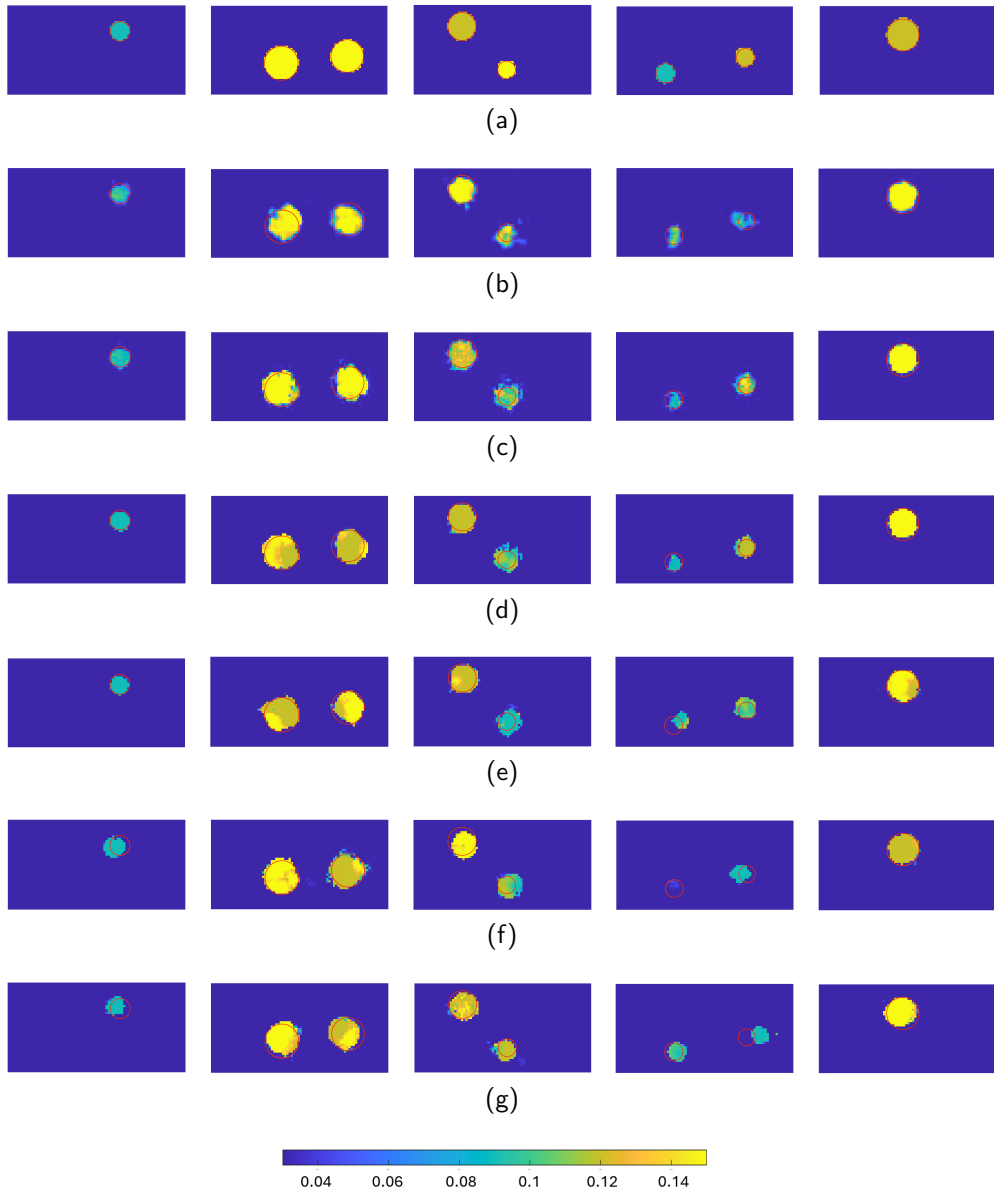


Fig. 14 Reconstruction of the absorption coefficient distribution obtained with the Mod-DOT approach. (a): ground truth; (b): reconstruction without pretraining the AEs, before the application of the denoiser; (c): reconstruction with pretraining of the AEs before denoising; (d): reconstruction with pretraining of the AEs after denoising. (e): 1% noise; (f): 3% noise; (g): 5% noise. Rows (e) to (g) use pretrain and denoising. Values are presented as μ_a/D , the red circles denote the true contrast regions.

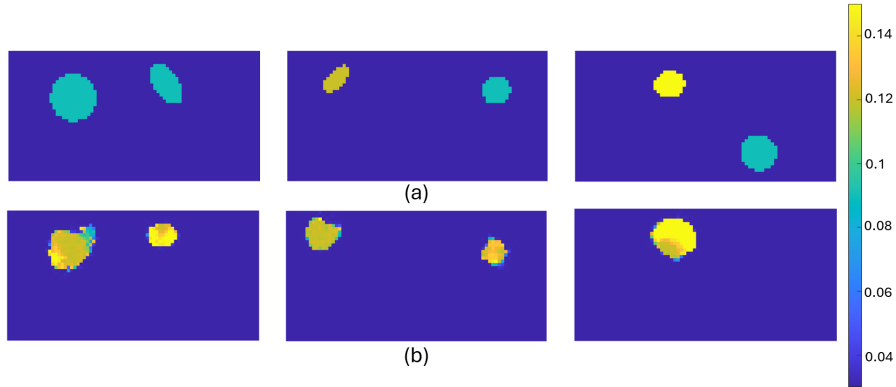


Fig. 15 Reconstruction of the absorption coefficient with out-of-distribution samples. Contrast regions have elliptical shapes with different locations, size and intensity. (a): ground-truth; (b): reconstruction obtained with the Mod-DOT approach trained on samples with only circular contrast regions. Values are presented as μ_a/D .

bridge-NN, which connects the data and signal latent spaces, also acts here as a learned regularizer of the inversion.

The Mod-DOT approach produces improved results with respect to classic approaches and also with respect to end-to-end neural network-based approaches. This is more evident for higher levels of noise, the more realistic situation, where the quality of the reconstruction remains acceptable.

Acknowledgments. Alessandro Benfenati and Paola Causin are part of the group GNCS (Gruppo Nazionale Calcolo Scientifico) of INdAM.

Author Contributions. All the authors equally contributed in the development of the model, MQ wrote the code and performed the numerical experiments. All the authors analyzed the results. PC wrote the paper, AB prepared Figs.8,9,10 and reviewed the manuscript.

Funding. We gratefully acknowledge the financial support of Italian MIUR–PRIN Grant 20225STXSB *Sustainable Tomographic Imaging with Learning and rEgularization (STILE)*

Availability of Data and Materials. All the implemented NN architectures are available upon reasonable request.

References

- [1] Y. Hoshi, Y. Yamada, Overview of diffuse optical tomography and its clinical applications. *Journal of Biomedical Optics* **21**(9), 091312 (2016)
- [2] Y. Yamada, S. Okawa, Diffuse optical tomography: Present status and its future. *Optical Review* **21**(3), 185–205 (2014)

- [3] H. Jiang, *Diffuse Optical Tomography: Principles and Applications* (CRC Press, 2018)
- [4] S.R. Arridge, Optical tomography in medical imaging. *Inverse Problems* **15**(2), R41 (1999)
- [5] T. Nielsen, T. Köhler, *Impact of noise-on-image reconstruction for diffuse optical tomography*, in *Medical Imaging 2006: Physics of Medical Imaging*, vol. 6142 (SPIE, 2006), pp. 200–207
- [6] J. Nocedal, S.J. Wright, *Numerical optimization* (Springer, 1999)
- [7] O. Lee, J.M. Kim, Y. Bresler, J.C. Ye, Compressive diffuse optical tomography: Noniterative exact reconstruction using joint sparsity. *IEEE Transactions on Medical Imaging* **30**(5), 1129–1142 (2011). <https://doi.org/10.1109/TMI.2011.2125983>
- [8] H.O. Kazanci, S.L. Jacques, *Diffuse light tomography to detect blood vessels using Tikhonov regularization*, in *Saratov Fall Meeting 2015: Third International Symposium on Optics and Biophotonics and Seventh Finnish-Russian Photonics and Laser Symposium (PALS)*, vol. 9917, ed. by E.A. Genina, V.V. Tuchin, V.L. Derbov, D.E. Postnov, I.V. Meglinski, K.V. Larin, A.B. Pravdin. International Society for Optics and Photonics (SPIE, 2016), pp. 202 – 210. <https://doi.org/10.1117/12.2230074>. URL <https://doi.org/10.1117/12.2230074>
- [9] S. Okawa, Y. Hoshi, Y. Yamada, Improvement of image quality of time-domain diffuse optical tomography with lp sparsity regularization. *Biomed. Opt. Express* **2**(12), 3334–3348 (2011). <https://doi.org/10.1364/BOE.2.003334>. URL <http://opg.optica.org/boe/abstract.cfm?URI=boe-2-12-3334>
- [10] P. Causin, G. Naldi, R. Weishaupl, *Elastic Net Regularization in Diffuse Optical Tomography Applications*, in *2019 IEEE 16th International Symposium on Biomedical Imaging (ISBI 2019)* (2019), pp. 1627–1630. <https://doi.org/10.1109/ISBI.2019.8759476>
- [11] P. Causin, M.G. Lupieri, G. Naldi, R.M. Weishaupl, Mathematical and numerical challenges in optical screening of female breast. *International Journal of Numerical Methods in Biomedical Engineering* **36**(2), e3286 (2020). <https://doi.org/https://doi.org/10.1002/cnm.3286>
- [12] A. Benfenati, P. Causin, M. Lupieri, G. Naldi, Regularization techniques for inverse problem in DOT applications. *Journal of Physics: Conference Series* **1476**, 012007 (2020). <https://doi.org/10.1088/1742-6596/1476/1/012007>
- [13] X. Zhang, M. Burger, S. Osher, A unified primal-dual algorithm framework based on Bregman iteration. *Journal of Scientific Computing* **46**(1), 20–46 (2011). <https://doi.org/10.1007/s10915-010-9408-8>

- [14] A. Benfenati, A. La Camera, M. Carbillet, Deconvolution of post-adaptive optics images of faint circumstellar environments by means of the inexact Bregman procedure. *Astronomy and Astrophysics* **586** (2016). <https://doi.org/10.1051/0004-6361/201526960>
- [15] A. Benfenati, V. Ruggiero, Inexact Bregman iteration with an application to Poisson data reconstruction. *Inverse Problems* **29**(6) (2013). <https://doi.org/10.1088/0266-5611/29/6/065016>
- [16] M. Schweiger, S.R. Arridge, The TOAST++ software suite for forward and inverse modeling in optical tomography. *Journal of Biomedical Optics* **19**(4), 040801 (2014)
- [17] Z. Wu, Y. Sun, A. Matlock, J. Liu, L. Tian, U.S. Kamilov, SIMBA: Scalable inversion in optical tomography using deep denoising priors. *IEEE Journal of Selected Topics in Signal Processing* **14**(6), 1163–1175 (2020). <https://doi.org/10.1109/JSTSP.2020.2999820>
- [18] Y. Romano, M. Elad, P. Milanfar, The little engine that could: Regularization by denoising (red). *SIAM Journal on Imaging Sciences* **10**(4), 1804–1844 (2017). <https://doi.org/10.1137/16M1102884>
- [19] R. Cohen, M. Elad, P. Milanfar, Regularization by denoising via fixed-point projection (red-pro). *SIAM Journal on Imaging Sciences* **14**(3), 1374–1406 (2021). <https://doi.org/10.1137/20M1337168>
- [20] P. Cascarano, A. Benfenati, U.S. Kamilov, X. Xu, Constrained regularization by denoising with automatic parameter selection. *IEEE Signal Processing Letters* pp. 1–5 (2024). <https://doi.org/10.1109/LSP.2024.3359569>
- [21] J. Yoo, S. Sabir, D. Heo, K. Kim, A. Wahab, Y. Choi, S.I. Lee, E. Chae, H. Kim, Y. Bae, Y.W. Choi, S. Cho, J. Ye, Deep learning diffuse optical tomography. *IEEE Transactions on Medical Imaging* **39**(4), 877–887 (2020). <https://doi.org/10.1109/TMI.2019.2936522>
- [22] M. Mozumder, A. Hauptmann, I. Nissilä, S.R. Arridge, T. Tarvainen, A model-based iterative learning approach for diffuse optical tomography. *arXiv preprint arXiv:2104.09579* (2021)
- [23] A. Aspri, A. Benfenati, P. Causin, C. Cavaterra, G. Naldi, Mathematical and numerical challenges in diffuse optical tomography inverse problems. *Discrete and Continuous Dynamical Systems-S* pp. 0–0 (2023)
- [24] Y.E. Boink, C. Brune, Learned SVD: solving inverse problems via hybrid autoencoding. *CoRR* **abs/1912.10840** (2019)

- [25] N. Franco, A. Manzoni, P. Zunino, A deep learning approach to reduced order modelling of parameter dependent partial differential equations. *Mathematics of Computation* **92**(340), 483–524 (2023)
- [26] J.K. Seo, K.C. Kim, A. Jargal, K. Lee, B. Harrach, A learning-based method for solving ill-posed nonlinear inverse problems: a simulation study of lung eit. *SIAM journal on Imaging Sciences* **12**(3), 1275–1295 (2019)
- [27] S. Lunz, O. Öktem, C.B. Schönlieb, *Adversarial regularizers in inverse problems* (2018), p. 8507 – 8516
- [28] E. Kobler, A. Effland, K. Kunisch, T. Pock, *Total Deep Variation for Linear Inverse Problems*, in *Proceedings of the IEEE/CVF Conference on Computer Vision and Pattern Recognition (CVPR)* (2020)
- [29] E. Kobler, A. Effland, K. Kunisch, T. Pock, Total deep variation: A stable regularizer for inverse problems. *CoRR* **abs/2006.08789** (2020). [2006.08789](https://arxiv.org/abs/2006.08789)
- [30] H. Li, J. Schwab, S. Antholzer, M. Haltmeier, NETT: solving inverse problems with deep neural networks. *Inverse Problems* **36**(6), 065005 (2020). <https://doi.org/10.1088/1361-6420/ab6d57>
- [31] J. Lorenzo, *Principles of diffuse light propagation: light propagation in tissues with applications in biology and medicine* (World Scientific, 2012)
- [32] L. Wang, H.I. Wu, *Biomedical optics: principles and imaging* (John Wiley & Sons, 2012)
- [33] C.F. Bohren, D.R. Huffman, *Absorption and scattering of light by small particles* (John Wiley & Sons, 2008)
- [34] J.L. Sandell, T.C. Zhu, A review of in-vivo optical properties of human tissues and its impact on pdt. *Journal of Biophotonics* **4**(11-12), 773–787 (2011)
- [35] A. Peraiah, *An Introduction to Radiative Transfer: Methods and applications in astrophysics* (Cambridge University Press, 2002)
- [36] S. Jacques, C. Alter, S. Prahl, Angular dependence of HeNe laser light scattering by human dermis. *Lasers Life Sci.* **1**, 309–333 (1987)
- [37] T. Durduran, R. Choe, W.B. Baker, A.G. Yodh, Diffuse optics for tissue monitoring and tomography. *Reports on progress in physics. Physical Society* **73** **7** (2010)
- [38] M. Mansuripur, *Classical optics and its applications* (Cambridge University Press, 2002)

- [39] A. Ishimaru, *Wave propagation and scattering in random media*, vol. 2 (Academic Press New York, 1978)
- [40] P. Causin, R.M. Weishaeufl, in *Mathematical Modelling in Real Life Problems* (Springer, 2020), pp. 1–16
- [41] D.A. Boas, T. Gaudette, S.R. Arridge, Simultaneous imaging and optode calibration with diffuse optical tomography. *Optics Express* **8**(5), 263–270 (2001)
- [42] S.D. Konecky, G.Y. Panasyuk, K. Lee, V. Markel, A.G. Yodh, J.C. Schotland, Imaging complex structures with diffuse light. *Optics Express* **16**(7), 5048–5060 (2008)
- [43] S. Arridge, P. Maass, O. Öktem, C.B. Schönlieb, Solving inverse problems using data-driven models. *Acta Numerica* **28**, 1–174 (2019). <https://doi.org/10.1017/S0962492919000059>. URL <https://doi.org/10.1017/S0962492919000059>
- [44] M. Benning, M. Burger, Modern regularization methods for inverse problems. *Acta Numerica* **27**, 1–111 (2018). <https://doi.org/10.1017/S0962492918000016>
- [45] H. Engl, M. Hanke, A. Neubauer, *Regularization of Inverse Problems*. Mathematics and Its Applications (Springer Netherlands, 1996)
- [46] G.P. Renieblas, A.T. Nogués, A.M. González, N. Gómez-Leon, E.G. Del Castillo, Structural similarity index family for image quality assessment in radiological images. *Journal of Medical Imaging* **4**(3), 035501–035501 (2017)
- [47] J. Friedman, T. Hastie, R. Tibshirani, Regularization paths for generalized linear models via coordinate descent. *Journal of Statistical Software* **33**(1), 1–22 (2010). URL <https://www.jstatsoft.org/v33/i01/>
- [48] R. Rockafellar, *Convex Analysis: (PMS-28)*. Princeton Landmarks in Mathematics and Physics (Princeton University Press, 2015)
- [49] J. Feng, Q. Sun, Z. Li, Z. Sun, K. Jia, Back-propagation neural network-based reconstruction algorithm for diffuse optical tomography. *Journal of Biomedical Optics* **24**(5), 051407–051407 (2019)
- [50] J. Yoo, S. Sabir, D. Heo, K. Kim, A. Wahab, Y. Choi, S.I. Lee, E. Chae, H. Kim, Y. Bae, et al., Deep learning diffuse optical tomography. *IEEE Transactions on Medical Imaging* **39**(4), 877–887 (2019)
- [51] B. Deng, H. Gu, S. Carp, *Deep learning enabled high-speed image reconstruction for breast diffuse optical tomography*, in *Optical Tomography and Spectroscopy of Tissue XIV*, vol. 11639 (International Society for Optics and Photonics, 2021), p. 116390B